MAASTY: A (dis)ordered copolymer for structural determination of human membrane proteins in native nanodiscs

Ciara F. Pugh[1], Lukas P. Feilen[1], Dušan Zivković[2], Kaia F. Præstegaard[3], Charalampos Sideris[3], Neil J. Borthwick[3], Casper de Lichtenberg[1], Jani R. Bolla[2], Anton A. A. Autzen[3*] & Henriette E. Autzen[1*]

Affiliations

[1]Department of Biomedical Sciences, University of Copenhagen, Copenhagen N, DK-2200, Denmark

[2]Department of Biology, University of Oxford, Oxford, OX1 3RB, United Kingdom

[3]Department of Health Technology, Technical University of Denmark, Kgs. Lyngby, DK-2800, Denmark

Corresponding authors

Anton A. A. Autzen (aaas@dtu.dk) & Henriette E. Autzen (henriette.autzen@sund.ku.dk)

Abstract

Amphiphilic copolymers capable of extracting membrane proteins directly from cellular membranes into ”native nanodiscs” offer a simplified approach for preparing membrane proteins in lipid nanodiscs compared to approaches that rely on detergent. Amphiphilicity, length, and composition influence the performance of copolymers, in addition to the protein itself and the purification conditions used. Here, we report a copolymer composed of methacrylic acid and styrene, which we term MAASTY, leveraging the inherent monomer reactivity ratios to create an anionic copolymer with a statistical distribution of monomers. We show that MAASTY can be used for high-resolution structural determination of a human membrane protein with single particle cryo-electron microscopy, preserving endogenous lipids including cholesterol and exhibiting an enrichment of phosphatidylinositol. Moreover, MAASTY copolymers effectively solubilize a broad range of lipid species and a wide range of different, eukaryotic membrane

proteins from mammalian cells. We find that MAASTY copolymers are promising as effective solubilizers of membrane proteins and offer a chemical platform for structural and functional characterization of membrane proteins in native nanodiscs.

Keywords: native nanodiscs, membrane protein structures, cryo-electron microscopy, polymer chemistry

Introduction

Integral membrane proteins represent an important class of therapeutic targets necessitating comprehensive understanding of their functional properties and structural attributes to facilitate rational drug development[1]. Specifically, structural characterization of integral membrane proteins has witnessed substantial progress the past decade, particularly driven by the technological advancements in single particle cryoelectron microscopy (cryo-EM)[2]. High-resolution cryo-EM has sparked an increased focus on reconstituting integral membrane proteins in lipid nanodiscs to effectively mimic native-like membrane environments[3]. The dominating approach for incorporating membrane proteins into lipid nanodiscs relies on detergent solubilization followed by subsequent re-lipidation, enabling the insertion of the membrane protein into a synthetic lipid bilayer encased by membrane scaffold proteins (MSPs) or saposin (Fig. 1a, black arrows)[4,5]. While reconstitution into synthetic nanodiscs facilitates the study of membrane proteins in a lipid environment, it inevitably comes at a cost of the native lipids, which are either partially or completely substituted by synthetic lipids. Consequently, only native lipids that exhibit exceptionally high affinity for the target protein remain associated with the reconstituted membrane protein[6–8]. Importantly, these reconstitution methods for the use of synthetic nanodisc systems disrupt the inherent asymmetry of the native membrane, may destabilize the membrane protein of interest through use of detergent-based extraction, and altogether, necessitate extensive and time-consuming optimization.

Nanodisc-forming copolymers, characterized by their amphipathic nature, have emerged as a promising alternative to traditional approaches for reconstituting integral membrane proteins into lipid nanodiscs[9–14]. These polymers are able to dissolve membranes and directly embed integral membrane proteins into what are coined ’native nanodiscs’, bypassing the requirement for initial detergent extraction before lipid

50 reconstitution (Fig. 1a, blue arrows). Although the native nanodisc method was established nearly two
51 decades ago[12], the method remains in an early stage of development; nevertheless, it has demonstrated
52 significant potential for cryo-EM studies and functional characterizations of various membrane proteins
53 expressed in both bacterial[9,15–17] and mammalian cells[18–22]. However, despite the promise of the native
54 nanodisc method, the limited number of high-resolution structures of membrane proteins embedded in
55 native nanodiscs indicates certain limitations inherent to the catalog of currently available copolymers.
56 The initial adoption of poly(styrene-co-maleic acid) (SMA) copolymers marked a significant milestone in
57 the development of the native nanodisc technology, and their continued utilization remains extensive[12,23–
58 25]. However, SMA suffers from notable drawbacks, such as its negative charge and high dispersity in
59 molecular weight, limitations that collectively restrict its applicability in structural and functional
60 characterization of membrane proteins[26–28]. Alternative copolymers aiming to address these challenges
61 include poly(diisobutyleneco-maleic acid) (DIBMA)[29], polymethacrylate (PMA)[30], stilbene-maleic
62 anhydride (STMA)[31], pentyl-inulin[32], poly(acrylic acid-co-styrene) (AASTY)[18], in addition to various
63 SMA derivative copolymers to mention a few[33–36].
64 Here, we explore the use of a copolymer for native nanodisc formation, poly(methacrylic acid-co-styrene)
65 composed of methacrylic acid (MAA) and styrene (STY), which we term MAASTY, and its applicability
66 toward forming native nanodiscs. We hypothesized that MAASTY copolymers act as effective nanodisc-
67 forming polymers on account of their structural similarity to SMA and AASTY and their highly
68 alternating behavior due to the reactivity ratios between MAA and STY in radical polymerizations.
69 MAASTY was developed on the framework of the copolymer AASTY[18], composed of acrylic acid (AA)
70 and STY, but differing by a methyl on the backbone of the acid bearing monomer (Fig. 1b). This methyl
71 influences the monomer reactivity ratios and the linear sequence of monomers in the resulting
72 copolymers, as well as their overall amphiphilicity due to the hydrophobicity of the methyl group. Similar
73 to AASTY, MAASTY can be synthesized by reversible addition-fragmentation chain-transfer (RAFT)
74 polymerization, allowing control of the copolymer length and the dispersity of size compared to free-
75 radical polymerization[37]. We decided to investigate MAASTY because of its moderately irregular

76 monomer composition and reduced composition drift in bulk polymerizations, enabling the exploration of
77 a broader range of homogeneous monomer compositions compared to AASTY.
78 We demonstrate that MAASTY can be used to extract and purify the human transient potential melastatin
79 4 (hTRPM4) ion channel from mammalian cells, allowing determination of its high-resolution structure
80 with single particle cryo-EM. Using fluorescent size-exclusion chromatography (FSEC), we show that
81 MAASTY copolymers extract a wide range of eukaryotic membrane proteins composed of different
82 numbers of subunits in native nanodiscs and form nanodiscs independent of the bulk lipid head group
83 charge, thus expanding the application potential of MAASTY copolymers across a variety of systems
84 with intricate membrane lipid compositions.

85 # Results

86 ## Synthesis and chemical characterization of MAASTY

87 Motivated by our previous work on AASTY copolymers[18,38], we synthesized six MAASTY copolymers
88 with a broad range of polymer compositions, varying the initial MAA monomer composition in the
89 reactions from 40-65% whilst aiming for a molecular weight between 7 and 8 kDa (Table 1). The
90 MAASTY copolymers are named according to their M_n (number-average molecular weight) and initial
91 MAA fraction. In radical polymerizations, a given monomer composition in a copolymerization will not
92 necessarily result in copolymers with identical polymer compositions due to relative differences in the
93 monomer reactivity ratios. This is evident from comparing the final MAA fraction (MAA frac) in the
94 polymers (Table 1) with the initial MAA fraction. Monomers are consumed at different rates, leading to a
95 composition drift of monomers along the chain. The composition drifts are simulated in Fig. 2a for
96 libraries of MAASTY and AASTY copolymers using their respective reactivity ratios (MAASTY; MAA:
97 0.4065, STY: 0.2911, AASTY; AA: 0.21, STY: 0.082)[39–41]. The copolymer composition drifts are
98 displayed for initial monomer compositions (40-65%) of MAA or AA. As shown in Fig. 2a, AASTY
99 initially has similar copolymer compositions across the simulated starting conditions due to its highly

alternating nature, resulting in a significant drift in polymer composition at higher conversions. The compositions of MAASTY, on the other hand, are more dispersed at all conversions. This moderately alternating nature of MAASTY is further highlighted by its determined simulated chemical correlation factor, λ, of approximately -0.5 for all tested copolymers (Table 1). This behavior is also apparent when comparing the regularity of monomer sequences as run lengths of each monomer (Fig. 2b). Here, a perfectly alternating copolymer would have a run length of 1, with any deviation indicating a higher degree of randomness. With a run length of 1.29, AASTY is highly alternating in terms of the monomer sequence, while MAASTY is more irregular with a run length of 1.68. A similar pattern can be observed in the product of the reactivity ratios (r_1r_2) for both copolymers, as r_1r_2 for AASTY is 0.017[41], whereas the r_1r_2 for MAASTY is 0.119[39]. Ultimately, this moderately alternating nature of the MAASTY co-polymerization allows for synthesis of a broader range of compositions without a significant drift in comparison to AASTY copolymerization.

We have previously shown that the charge state of the AASTY copolymer depends on the pH of the solution as acid groups are protonated at acidic pH values causing the polymer to become insoluble and unable to form lipid nanodiscs[18]. As MAASTY copolymers contain MAA groups, we decided to characterize the ionization state of the MAASTY copolymer library as a function of pH, identifying their respective pKa values and pH tolerances (Fig. S2; Table 1). The MAASTY copolymers displayed a single pKa in the range of 7.2-8.2. The broader polymer compositions give MAASTY copolymers an extended effective working pH range compared to AASTY copolymers with pKa values between 6.5 and 7.0 using initial AA fractions of 40%, 45%, 50% and 55%, respectively[18]. For MAASTY copolymers, the pKa decreases with increasing MAA fraction and correspondingly decreasing copolymer hydrophobicity (Table 1). This suggests that the solvation of phenyl moieties in water has a greater energetic barrier than the intra-chain charge repulsion from carboxylates. For instance, $MAASTY_{8.0}$-65 exhibits the lowest degree of protonation at lower pH values than the other MAASTY copolymers in the library indicating that this copolymer may be more effective in solubilizing lipids and proteins at a more acidic pH compared to a higher pH. Indeed, we see that $MAASTY_{8.0}$-65 performs better at pH 7 and 7.4 than 8 (Fig.

126 S3). It should be noted that all experiments in this study were carried out at pH 7.4, mimicking a
127 physiological pH; however, this may not be the optimal test conditions for the MAASTY copolymers on
128 either end of the MAA composition spectrum.
129 In addition to being pH sensitive, polyanionic copolymers are chelators of divalent cations through their
130 carboxylate moieties. This may cause complications when working with Ca^{2+} or Mg^{2+}-dependent proteins
131 in polymer-stabilized nanodiscs. Consequently, we assessed the Ca^{2+} sensitivity of MAASTY copolymers
132 using a colorimetric detection assay of free Ca^{2+} ions with *o*-cresolphthalein complexone (oCPC), as
133 carried out previously for AASTY[38]. oCPC yields a bright purple complex with an absorbance maximum
134 at 575 nm upon chelating divalent cations, allowing a measurement of the free Ca^{2+} ions left in solution
135 following copolymer exposure (Fig. S4a, b). For the tested MAASTY copolymers, the total escaped Ca^{2+}
136 ions remained consistent at 1.2 ± 1.5 % for the 1 mM and 3 mM $CaCl_2$ conditions (Fig. S4c). We
137 measured a sudden increase to 5.1 ± 0.8 % of total escaped Ca^{2+} ions with 7 mM added $CaCl_2$ for all
138 copolymers except $MAASTY_{7.0}$-45. This increase may occur as the copolymer becomes saturated with
139 Ca^{2+} at this concentration. Overall, a higher absolute copolymer MAA fraction does not equate to higher
140 Ca^{2+} binding capacity, within the concentration range tested. This is similar to what we found previously
141 for AASTY copolymers[38]. Contrarily, the affinity of MAASTY copolymers for Ca^{2+} is seemingly higher
142 than AASTY, given a drastically different 21% of total escaped Ca^{2+} ions was measured for equivalent
143 assayed concentrations in the presence of AASTY[38]. This lower Ca^{2+} tolerance of MAASTY compared to
144 AASTY may be due to its increased hydrophobicity, resulting in Ca^{2+} being kinetically trapped within
145 solubilized aggregates of MAASTY-Ca^{2+} complex.
146 To further understand the impact of divalent cations on the nanodisc-forming ability of MAASTY
147 copolymers, we produced fluorescent nanodiscs by solubilizing small unilamellar vesicles (SUVs)
148 composed of 1-palmitoyl-2-oleoyl-*sn*-glycero-3-phosphocholine (POPC) and 2% fluorescent 1,2-
149 dioleoyl-*sn*-glycero-3-phosphoethanolamine-N-(lissamine rhodamine B sulfonyl) (LissRhod)
150 phosphatidylethanolamine (PE) with MAASTY copolymers in the presence of specific $CaCl_2$ and $MgCl_2$
151 concentrations and subjected them to FSEC (Fig. S5). As previously exhibited for SMA and AASTY

152 copolymers[27,38], solubilization by MAASTY copolymers is more sensitive to Ca^{2+} ions than Mg^{2+} ions.
153 Additionally, as divalent cation concentrations increase, the fraction of larger soluble species also
154 increases, a phenomenon that may be caused by rouleaux stacking of nanodiscs under these conditions[42].
155 In contrast to the free copolymer assessed in the oCPC assay (Fig. S4), the tolerance towards Ca^{2+} and
156 Mg^{2+} ions during nanodisc-formation appears to depend on copolymer composition. Of note, MAASTY
157 copolymers with higher MAA content than STY ($MAASTY_{8.2}$-55, $MAASTY_{8.1}$-60 and $MAASTY_{8.0}$-65)
158 were observed to better tolerate the presence of divalent cations during nanodisc-formation, solubilizing
159 lipids either as well or to a greater extent in the presence of Ca^{2+} or Mg^{2+} ions (Fig. S5g).

160 MAASTY facilitates high-resolution structural determination of integral membrane 161 proteins

162 To benchmark the utility of MAASTY copolymers for structural determination of integral membrane
163 proteins, we screened the solubilization capacity of our MAASTY copolymer library on full-length
164 hTRPM4, N-terminally tagged with StrepTag-IIeGFP, and recombinantly expressed in HEK293 cells
165 with FSEC (Fig. S6) and compared it to detergent-solubilization (Fig. S7). hTRPM4 is a Ca^{2+}-activated,
166 non-selective monovalent cation channel that is broadly expressed and contributes to the pathophysiology
167 of cardiovascular diseases, prostate cancer, and diseases of the central nervous system[43]. Notably,
168 solubilization with MAASTY outperforms DDM-CHS (Fig. S7). In accordance with FSEC screening of
169 the MAASTY copolymer library, hTRPM4 was solubilized and purified in $MAASTY_{7.1}$-50 nanodiscs
170 (Fig. S6; S8; S9), and subjected to single-particle cryo-EM analysis, resulting in a structure with an
171 overall resolution of 3.5 Å (Fig. 3a; Fig. S10; S11; Table S1). The transmembrane domain and
172 extracellular loops, the N-terminal, cytosolic TRPM homology region 4 (MHR4) and the central coiled-
173 coil in the C-terminus were well-resolved, and overall identical to previously determined cryo-EM
174 hTRPM4 structures in detergent micelles or MSP nanodiscs[44–47]. Despite extensive 3D classifications and
175 focused refinements imposing either C1 or C4 symmetry, the portions of the cytosolic domain composed

176 by the MHR1-3 of hTRPM4 in MAASTY nanodiscs were unresolved, likely due to conformational
177 flexibility under the experimental conditions (Fig. 3b). Structural flexibility of this part of the cytosolic
178 domain is also evident from the structure of hTRPM4 in MSP2N2 nanodiscs performed in parallel with
179 hTRPM4 in MAASTY nanodiscs (Fig. S12; S13) and as previously described[45], albeit not as severe as in
180 MAASTYstabilized nanodiscs. Notably, a recent structure of hTRPM4 in SMA nanodiscs also resulted in
181 an unresolved cytosolic region of MHR1-2[21], underscoring that hTRPM4 is more flexible in copolymer-
182 based lipid nanodiscs, possibly due to larger heterogeneity in the lipid composition compared to the
183 reconstituted MSP nanodisc system and detergent micelles or, in part, due to differences in lipid packing
184 protection provided by the nanodisc-stabilizing copolymers or proteins.
185 From analyzing the hTRPM4-MAASTY structure, we found several extra densities that we identified as
186 lipids (Fig. 3c). Along with observing densities of lipids, we modelled three densities as cholesterol
187 (CLR) molecules due to its distinct shape and location (Fig. 3d). The identified CLR molecules in site 1
188 and site 2 (CLR-1 and CLR-2, respectively) lie within sites previously annotated as cholesteryl
189 hemisuccinate (CHS) binding sites by Autzen *et al.*[45], and discerned in the hTRPM4-MSP2N2 structure
190 of this study (Fig. S12; S13). CLR-1 is located at the pre-S1 elbow, creating a cavity with S1, S4 and
191 MHR4 helix 7, and CLR-2 lines the pore, interacting with the pore helix and S6, supposedly stabilizing
192 the pore conformation[45]. CLR site 3 (CLR-3) is situated between S1, S5 and the pore helix of the adjacent
193 proteomer, and was also observed in the structure of hTRPM4 in SMA nanodiscs[21]. Both hTRPM4
194 structures determined in SMA[21] and MSP2N2[45], including this study, identified CLR or CHS in a binding
195 site that corresponds to the vanilloid binding pocket of TRPV1[48]. We also observed a similar density at
196 that location in the hTRPM4-MAASTY structure, however due to low occupancy, we were unable to
197 definitively model it as CLR.
198 In order to assess the endogenous lipid species co-purified with hTRPM4 in MAASTY native nanodiscs,
199 we extracted the lipids from the purified sample and analyzed it with MALDI-TOF mass spectrometry
200 (MS). This confirmed the presence of CLR in the nanodiscs, in addition to POPC (Fig. S14). As a further,
201 in-depth evaluation of the relative abundance of the extracted lipid species, we subjected the hTRPM4-

202 MAASTY nanodisc sample to lipidomics analysis. This identified a variety of putative endogenous lipid
203 species co-extracted with hTRPM4 (Fig. S15), including lipids belonging to the phospholipid classes
204 phosphatidylinositol (PI), phosphatidylcholine (PC), phosphatidylethanolamine (PE),
205 phosphatidylglycerol (PG) and phosphatidylserine (PS). PE, PI and PC constituted a majority of the
206 identified lipid classes. The lipidomics analysis also detected plasmenyl-, plasmanyl- and
207 lysophospholipids, highlighting the complexity of membrane lipid species stabilizing, and possibly
208 regulating, hTRPM4 in an endogenous lipid environment.
209 Interestingly, the MAASTY nanodisc encapsulating hTRPM4 exhibits a distinct shape. When looking
210 down the ion channel pore axis, the nanodisc is observed as a ”square” with an overall shape similar to
211 the transmembrane domain of hTRPM4 itself, rather than circular as for hTRPM4 in MSP2N2 nanodiscs
212 (Fig. 3a; S12b)[45]. This resolved nanodisc shape was also observed for hTRPM4 in SMA nanodiscs[21],
213 appearing as an extension of the shape formed by the TM domains themselves, and likely derived from
214 the higher degrees of freedom in flexibility of the copolymer compared to, for example, the rigidity of
215 MSP helices. This is an attribute shared by other resolved cryo-EM structures of copolymer-encapsulated
216 nanodiscs[16,49,50]. Despite the discrepancy in nanodisc shapes, the transmembrane domains were identical
217 between the hTRPM4 structures in MAASTY and MSP2N2 nanodiscs with matching pore profiles (Fig.
218 3e).
219 Next, we sought to estimate the composition of the hTRPM4-MAASTY particles. The mass contribution
220 from the individual components in the nanodisc is apparent when assessing the sample by mass
221 photometry (MP) and spectroscopic quantification of hTRPM4 and MAASTY copolymers in the
222 nanodiscs. MP of hTRPM4 in MAASTY revealed a peak around 760 kDa (Fig. S8c). Subtracting the
223 mass of hTRPM4 (540 kDa for the cleaved tetramer), the excess mass of approximately 220 kDa may be
224 attributed to extracted lipids and surrounding copolymers of the nanodisc. To assess the composition of
225 the solubilized particles, we solubilized and purified hTRPM4 in $MAASTY_{7.1}$-50 with a trithiocarbonate
226 (ttc) moeity at the terminal, which has a maximum absorbance at 310 nm, and quantified hTRPM4-
227 $MAASTY_{7.1}$-50_{ttc} with FSEC and the Bradford protein assay (Fig. S8d, e). We estimate that for each

228 solubilized particle, the copolymer contributes approximately 110 kDa, with 110 kDa remaining as
229 contribution from lipids. At the molecular level, this means that every hTRPM4-MAASTY particle
230 contains an average of 13 MAASTY copolymers.
231 Finally, from analysis of the hTRPM4-MAASTY structure, we observed an apparent density representing
232 a Ca^{2+} ion in the established Ca^{2+}-binding site (Fig. 3f), coordinated by side chain groups of Glu^{828}, Gln^{831},
233 Asn^{865} and Asp^{868} located at the S2-S3 helices[44,45,47]. This observation indicates that hTRPM4 in
234 MAASTY nanodiscs can capture endogenous Ca^{2+} without the need to supplement it throughout
235 purification or cryo-EM sample preparation. Moreover, it lends promise to the potential use of MAASTY
236 copolymers to characterize divalent cation-bound membrane proteins despite being polyanionic.

237 MAASTY solubilizes a diverse test set of membrane proteins

238 Next, we assessed the the versatility of the MAASTY copolymers across varying protein types through
239 the solubilization of three additional eukaryotic integral membrane proteins, fused with eGFP, and
240 recombinantly expressed in HEK293 cells. The test set included three differing oligomeric configurations,
241 represented by the rabbit sarco/endoplasmic reticulum Ca^{2+}-ATPase 1a (rSERCA1a, monomeric), the
242 human potassium channel subfamily K member 18 (hKCNK18, homodimeric), and the chicken acid
243 sensing ion channel 1 (cASIC1, homotrimeric), in addition to the homotetrameric hTRPM4 presented in
244 the previous section (Fig. S6). For each membrane protein, we compared the solubilization efficacy of the
245 MAASTY copolymer library with a selection of six AASTY copolymers with initial AA content of 45%,
246 50% and 55% and masses of either 6 kDa or 11 kDa, respectively (Fig 4; Table S2; Fig. S16).
247 rSERCA is a P-type ATPase that pumps Ca^{2+} ions from the cytoplasm into the sarcoplasmic or
248 endoplasmic reticulum, and plays a critical role in muscle contraction and cellular Ca^{2+} homeostasis[51].
249 With 79 deposited models in the PDB, rSERCA is structurally and functionally well-characterized.
250 Solubilization of rSERCA1a with both MAASTY and AASTY copolymers, produced a largely
251 monodisperse peak with a trailing shoulder at longer retention times (Fig. S16a). $MAASTY_{7.4}$-40 and
252 $MAASTY_{7.0}$-45 were most effective at solubilizing rSERCA1a, with decreasing solubilization efficiency

253 as the MAA content of the copolymer increased, with two of six MAASTY copolymers performing worse
254 than the best AASTY copolymer (Fig. 4b; Fig. S16a). While most of the copolymers showed the same
255 retention times, three of the MAASTY copolymers, $MAASTY_{8.2}$-55, $MAASTY_{8.1}$-60, and $MAASTY_{8.0}$-
256 65 showed slightly earlier retention times, which may be indicative of larger discs compared to the later
257 eluting species (Fig. S16a).
258 hKCNK18 is a potassium channel implicated in regulation of neuronal excitability and associated with
259 certain types of migraines[52]. The structure of hKCNK18 is yet to be determined, probably due to
260 difficulties in its expression and stabilization outside the cell membrane. For hKCNK18, all MAASTY
261 copolymers led to FSEC traces with shoulders, making it difficult to estimate the solubilization efficacy
262 and the retention volumes (Fig. S16b). $MAASTY_{7.0}$-40 seemingly displayed the highest solubilization
263 capacity, producing a more uniform peak than the five other MAASTY copolymers and any of the tested
264 AASTY copolymers (Fig 4b; Fig. S16b).
265 cASIC1 is a proton-gated Na^+ channel involved in detection of acidic environments. With approximately
266 90% sequence identity to human ASIC1a, a protein implicated in a variety of neuropathologies[53], cASIC1
267 is the most structurally well-characterized of the ASICs amounting to 19 deposited models in the PDB. A
268 majority of these were determined in detergent micelles, but some were resolved in SMA[19]. For cASIC1,
269 both MAASTY and AASTY copolymers acted as effective solubilizers, generating a uniform presumed
270 protein-nanodisc peak with a trailing shoulder on the right side of the main peak (Fig. S16c).
271 $MAASTY_{7.0}$-45 and $MAASTY_{7.1}$-50 were the most potent solubilizers, however, most of the MAASTY
272 copolymers solubilized cASIC almost as well (Fig. 4b). As with rSERCA1a, four of six MAASTY
273 copolymers produce higher peak intensities than the best-performing AASTY copolymer. Interestingly,
274 there was a distinct difference in retention volumes between MAASTY and AASTY copolymer nanodiscs
275 for cASIC1, with MAASTY copolymers eluting at earlier volumes forming evidently larger cASIC1-
276 containing nanodiscs than AASTY copolymers (Fig. S16c). This may also be the case for hKCNK18,
277 indicating a possibility that MAASTY copolymers form larger protein-containing nanodiscs than AASTY
278 copolymers.

MAASTY is compatible with a broad selection of lipids

As previously described, the efficiency of nanodisc formation by AASTY copolymers is highly dependent on membrane charge, specifically favoring more zwitterionic lipid compositions[18], whereas the anionic SMA and DIBMA copolymers reportedly solubilize irrespective of lipid charge[54–56]. To assess the effect of lipid composition on MAASTY solubilization, we dissolved 2% fluorescent LissRhod PE and one of three lipid mixtures: POPC, soy polar lipid extract (PLEx) and *E. coli* PLEx with MAASTY copolymers to form protein-free or ”empty” nanodiscs. Using FSEC, we determined the lipid solubilization capacity for each MAASTY copolymer from the fluorescence intensity (Fig. 5; Fig. S17). All six MAASTY copolymers formed nanodiscs with all three lipid compositions, and although the efficiencies vary, the MAASTY library forms nanodiscs with both the synthetic lipid POPC and the two lipid extracts (Fig. 5b). This is in contrast to AASTY, which showed significantly decreased efficiency for soy PLEx and *E. coli* PLEx, likely owing to their content of charged lipid species[18]. From the MAASTY library, $MAASTY_{7.0}$-45 and $MAASTY_{7.1}$-50 were the most effective copolymers for all three of the tested lipid compositions. In contrast, $MAASTY_{8.0}$-65, which is the copolymer with the highest MAA fraction (63%), was the least effective at solubilizing the three lipid compositions. $MAASTY_{8.0}$-65 was particularly poor at solubilizing *E. coli* PLEx, which has a high content of negatively charged lipid species such as cardiolipin (~10%) and phosphatidylglycerol (~23%); This could be a charge effect as $MAASTY_{8.1}$-60, with the second highest MAA fraction (59%), also displayed a diminished capacity to solubilize *E. coli* PLEx (Fig. 5b). Indeed, with pKa values at 7.2 and 7.4, respectively, these two copolymers are likely either predominantly charged or at least 50% charged at pH 7.4 (Table 1; Fig. S2).

Notably, we observed a disparity in retention volumes across the tested MAASTY copolymers and lipid compositions (Fig. 5c). Overall, there appears to be a trend of lower retention volumes with increasing copolymer MAA content. For example, $MAASTY_{8.0}$-65, which has the highest MAA fraction of all tested copolymers, has the smallest retention volumes, particularly when forming nanodiscs of POPC and *E. coli* PLEx. In general, POPC and *E. coli* PLEx containing nanodiscs display lower retention volumes than soy

304 PLEx for each of the MAASTY copolymers, except $MAASTY_{7.4}$-40. Whether the dissimilarity in
305 retention volume is an indication of differences in the relative disc sizes, i.e. a creation of larger nanodiscs
306 from lower retention volumes, or rather a result of the charge state of the polymer, remains to be assessed
307 further.

308 ## Discussion

309 The limited number of structural studies of membrane proteins in native nanodiscs underscores a
310 requirement to improve our current repertoire of nanodisc-forming copolymers. Only recently did the first
311 high resolution structures of human membrane proteins in native nanodiscs emerge, emphasizing the
312 potential of the method[21,22]. Here we introduce the copolymer MAASTY, which can solubilize membrane
313 proteins in native nanodiscs and facilitate high-resolution structural determination. We previously
314 conceptualized AASTY as an effective copolymer for formation of native nanodiscs, based on the
315 structural regularity of this copolymer[18]. Since then, it was found that altering the hydrophobicity of the
316 styrenic moiety of alternating SMA copolymers also yields effective nanodisc forming copolymers[57]. On
317 this basis, we envisioned that changing AA to MAA could result in an improvement, as the methyl group
318 of MAA is more hydrophobic. Previous research into nanodisc forming copolymers shows that the main
319 properties determining nanodisc-forming capabilities are the amphiphilicity, size, monomer sequence and
320 monomer composition of the copolymers[57–60]. Delineating the effects of these four properties on nanodisc
321 formation is non-trivial as exchanging a monomer with another results in a different statistical distribution
322 of monomers along the chain (Fig. 2). Our rationale for designing AASTY and our hypothesis on why it
323 is an effective solubilizer was that the alternating monomer sequence, in combination with a similar
324 amphiphilicity to effective SMA compositions, would be more effective than SMA due to the high
325 regularity in monomer sequence[18]. As such, we were somewhat surprised that MAASTY, which is more
326 irregular than AASTY, proved to be as effective in nanodisc-formation and, for some targets, seemingly
327 performed better than AASTY. However, by using MAA instead of AA, we change both the
328 amphiphilicity and the statistical distribution of monomers in the polymer, emphasizing that observed
329 differences between MAASTY and AASTY, or other copolymers for that matter, with regard to nanodisc
330 formation cannot be attributed to one particular polymer property. The key difference of MAASTY to
331 AASTY is the increased hydrophobicity of MAASTY, and it could be that the packing of the methyl
332 group into the lipid bilayer is beneficial for the stabilization of nanodiscs. As polymers with methylated
333 backbones have lower glass transition temperatures than their non-methylated acrylate counterparts, this

334 feature could result in a more rigid structure, conferring higher stability of the disc. The more
335 hydrophobic nature of the MAASTY copolymers will also likely result in increased sensitivity to divalent
336 cations, at least for the free copolymers, as the charge of the carboxylates are neutralized by Ca^{2+} ions,
337 resulting in precipitation. We hypothesize that this is the reason for the pronounced Ca^{2+} ion binding we
338 see with MAASTY copolymers in the oCPC assay (Fig. S4). Furthermore, the large span of pKa values
339 for the MAASTY copolymer library synthesized in this study is a result of the wider range of
340 compositions enabled by the less-alternating nature of the copolymerization in comparison to AASTY
341 (Table 1). More MAA in a copolymer results in a markedly lower pKa, which can only mean that the
342 energy penalty for deprotonating MAA afforded by the local hydrophobic environment of STY moieties
343 is larger than the penalty from adjacent negative charges from deprotonated carboxylates. In practice
344 however, this likely means that MAASTY copolymers can be tailored to perform optimally at a desired
345 pH.

346 The high-resolution cryo-EM structure of hTRPM4 in MAASTY native nanodiscs showcases the
347 applicability of MAASTY copolymers and expands the toolbox for membrane protein characterization
348 (Fig. 3; 4). The structure elaborates on our previous research on AASTY copolymers in which sample and
349 conformational heterogeneity yielded low-resolution reconstructions of hTRPM4 in native nanodiscs[18].
350 There may be many possible explanations for the successful use of MAASTY for high-resolution
351 structural determination of hTRPM4 by cryo-EM in comparison to AASTY, such as altered orientational
352 distribution, number of particles at the air-water interface and conformational flexibility resulting from
353 differences in overall charge of the protein-nanodisc complex. In addition, we cannot exclude that a high
354 resolution structure with AASTY may have been feasible to obtain from a larger dataset. It is also
355 possible that potential differences in the co-purified lipids between AASTY and MAASTY contribute to
356 the success of MAASTY for the structural determination of hTRPM4. Indeed, lipid solubilization with
357 MAASTY and AASTY show different lipid preferences for the two copolymers; AASTY displayed a

358 lower propensity to solubilize negatively-charged lipids[18], while MAASTY solubilizes lipids
359 independently of head-group charge (Fig. 5).

360 According to lipidomics analysis of hTRPM4-MAASTY nanodiscs, two of the top five most abundant
361 lipid species co-extracted with hTRPM4 are the negatively charged lipid species PI and PS (Fig. S15).
362 Notably, with an observed relative abundance of 15-25%, PI co-purified in hTRPM4-MAASTY
363 nanodiscs far exceeds the typical plasma membrane content of 1-2%[61]. Whether the enrichment of PI and
364 PS is due to hTRPM4, the HEK293 cells or the MAASTY copolymers should be further tested. Along
365 with its reported role in channel regulation, the phosphorylated PI, phosphatidylinositol 4,5-bisphosphate
366 (PIP2), has been hypothesized to aid in conformationally stabilizing hTRPM4[62,63]. We speculate that
367 differences in extraction of charged lipids between AASTY and MAASTY copolymers may have resulted
368 in less co-purified PI in the hTRPM4-AASTY sample, along with other negatively-charged lipids,
369 consequently displaying increased conformational heterogeneity and potentially contributing to the
370 yielding of a lower resolution structure, among other aformentioned possibilities. Furthermore, other
371 lipids such as CLR may be necessary to stabilize hTRPM4[18,44–46,64]. The stability of the transmembrane
372 domain by lipids may also play a role in the missing cytosolic MHR1-3 domains in the hTRPM4-
373 MAASTY structure which we assume is caused by structural flexibility. This structural flexibility could
374 even be potentiated by the copolymers themselves either through direct or indirect interactions with the
375 protein. Indeed, this has been reported for membrane proteins in MSP nanodiscs whereby amphipathic
376 interactions with the MSP may influence the local dynamics of the membrane protein[65]. Lastly,
377 MAASTY copolymers consistently solubilize hTRPM4 to a greater extent than AASTY copolymers, with
378 $MAASTY_{7.1}$-50 as the most efficacious, potentially contributing to better sample quality (Fig. S6).
379 hTRPM4 solubilization by $MAASTY_{7.1}$-50 was even shown to outperform DDM-CHS (Fig. S7).

380 Endogenous lipids are clearly visible in the hTRPM4-MAASTY structure and further confirmed by
381 lipidomics analyses (Fig. 3; S14; S15). The observed arrangement of lipid densities in the hTRPM4
382 MAASTY structure differed from that of hTRPM4 in MSP2N2. Specifically, we identified the locations

383 of three CLR binding sites; two of which are also occupied in the hTRPM4-SMA structure[21], and a novel
384 location previously annotated as a CHS-binding region[45], adding to our current knowledge on lipid
385 organization in hTRPM4. MS analyses highlighted the complexity of the co-purified endogenous lipid
386 species unassigned in the hTRPM4-MAASTY structure. These identified lipids may be implicated in
387 hTRPM4 activity, regulation, and/or stabilization. For example, the detection of lysophospholipid classes
388 could indicate a potential role in channel modulation, as established in other TRP channels[66,67].

389 In addition to endogenous lipids, hTRPM4 in MAASTY nanodiscs were bound to endogenous Ca^{2+} ions,
390 according to an observed density in the Ca^{2+}-binding site without having supplemented the sample with
391 $CaCl_2$ during purification or cryoEM sample preparation. The binding of Ca^{2+} from an endogenous source
392 was also eluded to in the hTPRM4-SMA structure[21], while this was not reported for any of the detergent-
393 solubilized structures[44–46,64]. The ability to capture a Ca^{2+}-bound state of hTRPM4 gives evidence towards
394 the use of MAASTY copolymers to characterize divalent cation sensitive membrane proteins despite the
395 polyanionic nature of MAASTY and consequent propensity to bind Ca^{2+}. Indeed, we show that
396 MAASTY-encasing protein-free nanodiscs are tolerant of $CaCl_2$ and $MgCl_2$ (Fig. S5). These observations
397 underscore the importance of assessing tolerance to solvent compositions, such as the addition of divalent
398 cations, under nanodisc-forming conditions, as opposed to solely measuring the impact on free copolymer
399 (Fig. S4). While the enhanced tolerance of higher MAA content copolymers suggest they may be
400 particularly well suited for studying Ca^{2+} or Mg^{2+} sensitive proteins, this is likely also influenced by the
401 properties of the solubilized membrane protein. In general, the decrease in accessible divalent cations by
402 copolymer chelation, and consequent concentration change throughout membrane protein purification, are
403 both essential effects to be aware of.

404 Finally, we demonstrate that MAASTY is a versatile copolymer capable of solubilizing a range of
405 disease-relevant membrane proteins and diverse lipid compositions (Fig. 4; 5). Interestingly, we noted
406 differences in SEC elution volumes between MAASTY and AASTY nanodiscs incorporating membrane
407 proteins, as well as retention volume differences for MAASTY-encasing protein-free nanodiscs of

408 increasing negatively-charged lipid compositions. These observations indicate that solubilization efficacy
409 is dependent on the membrane protein solubilized, the lipid species, and the copolymer itself.

410 While it is unlikely that there is a one-size-fits-all solution of nanodisc-forming copolymers, MAASTY is
411 an easily synthesized copolymer, able to yield a high resolution structure in a nanodisc without the need
412 for extensive reconstitution optimization. Understanding the mechanism of how MAASTY and other
413 copolymers work will ease the identification of which copolymers are effective for specific protein targets
414 in a given membrane composition. Further lipidomics analyses of native nanodiscs could help elucidate
415 how lipids influence other target-copolymer combinations. We conclude that our work showcases the
416 potential of MAASTY in membrane protein biochemistry and structural biology, and lends promise to its
417 further use in the field as an effective solubilizer of integral membrane proteins in native lipid nanodiscs
418 across varying recombinant-expression and native systems.

419 # Methods

420 ## Synthesis and characterization of MAASTY copolymers

421 Methacrylic acid (MAA) and styrene (STY) were distilled under vacuum. The RAFT agent 2-Methyl-2-
422 [(dodecylsulfanylthiocarbonyl)sulfanyl]propanoic acid (194 mg, 0.531 mmol) and azobisisobutyrunitrile
423 (17.4 mg, 0.106 mmol) were added to six ampules. Styrene and methacrylic acid were added to the
424 ampules; MAASTY$_{7.4}$-40 (MAA: 1.7 mL, 1.7 g, 20 mmol, STY: 3.44 mL, 3.13 g, 30 mmol),
425 MAASTY$_{7.0}$-45 (MAA: 1.91 mL, 1.94 g, 22.5 mmol, STY: 3.15 mL, 2.85 g, 27.5 mmol), MAASTY$_{7.1}$-
426 50 (MAA: 2.12 mL, 2.15 g, 25 mmol, STY: 2.86 mL, 2.60 g, 25 mmol), MAASTY$_{8.2}$-55
427 (MAA: 2.33 mL, 2.37 g, 27.5 mmol, STY: 2.58 mL, 2.34 g, 27.5 mmol), MAASTY$_{8.1}$-
428 60 (MAA: 2.55 mL, 2.60 g, 30 mmol, STY: 2.29 mL, 2.10 g, 20 mmol), MAASTY$_{8.0}$-65 (MAA: 2.76
429 mL, 2.80 g, 32.5 mmol, STY: 2.05 mL, 1.82 g, 18.5 mmol). The ampules were degassed by four freeze-
430 pump-thaw cycles, and sealed under vacuum while frozen. They were then placed in a water bath in a 60
431 °C oven for 17h, forming yellow solids. The solids were removed by ampule shattering and each

432 dissolved in 10 mL absolute ethanol. At this point, samples for determining conversion by NMR were
433 taken. 20 equiv. of H_2O_2 (30% in water) was added with respect to end-groups. These mixtures were
434 heated to 70 °C overnight resulting in non-colored solutions. The solutions were precipitated into heptane
435 and the white precipitate was recovered by filtration. The polymers were converted to their respective
436 sodium salts by suspending them in ultrapure water and titrating in 1 M NaOH until the pH was stable at
437 approximately pH 8.0, and the bulk of the suspended polymer was dissolved. These solutions were
438 filtered through 0.22 µM PES syringe filters and freeze-dried.

439 Bjerrum diagrams were constructed by dissolving 50 mg of respective polymer in 10 mL water and
440 adjusting the pH to approximately 11 with 1 M NaOH. 0.33 M HCl solution was titrated in 5 µL
441 increments whilst measuring the pH on a Mettler Toledo SevenCompact S210 pH meter.

442 We were unable to use aqueous SEC Multi-Angle Light static Scattering (MALS) to characterize the
443 MAASTY copolymers. Even at minimal concentration, MALS would report masses that were orders of
444 magnitude higher, than expected for the given elution time. Expecting these effects were due to
445 micellization, we performed the analysis in organic SEC, after methylation, as previously described[68]. The
446 analysis showed a greater dispersity than what could be expected for RAFT made polymers. We believe
447 that this is due to incomplete methylation resulting in aggregation or crosslinking of polymers.

448 NMR characterization of MAASTY

449 Conversion of monomers were determined by ^{1}H-NMR using a Bruker Avance III 400 MHz system using
450 d6-DMSO and a probe temperature of 25 °C. The ^{1}H-NMR of the purified polymers converted to sodium
451 salts were obtained in D_2O (Fig.S1).

452 Methylation and SEC characterization of MAASTY polymers

453 MAASTY polymer (1 equiv.) was suspended in a 1 w% 1-methyl-3-*p*-tolyltriazene (MTT) solution (1.2
454 equiv.) in toluene. The mixture was left to stir overnight. The reaction was finished when all polymer had

455 dissolved in the toluene. Once the reaction was finished, the toluene was washed twice with 1 M HCl and
456 the solvent was removed under vacuum. The degree of methylation was confirmed with NMR.
457 Methylated MAASTY was dissolved in THF to a concentration of 2.5 mg/mL. Measurements were
458 performed on a Viscotek Differential Refractometer viscometer with SIL-10AD VP Shimadzu
459 Autosampler and LC-10ADVP Shimadzu Pump using THF as solvent and PLgel 3um MIXED E Column
460 of 300 mm x 7.5 mm cross-linked porous polystyrene divinylbenzene matrix from Polymer Laboratories.

461 Determination of free Ca^{2+} concentrations

462 To measure the concentration of free Ca^{2+} ions in the presence of MAASTY, copolymers were mixed with
463 buffer for a final composition of 20 mM HEPES/NaOH (pH 7.4), 100 mM NaCl, and 0, 1, 3, or 7 mM
464 $CaCl_2$ and either 0.1% or 1% weight per volume (w/v) copolymer. After 15 min of incubation, ~10 µL of
465 buffer without copolymer was isolated using a Vivaspin-500 centrifugal concentrator with a 10 kDa
466 MWCO cutoff. In a 96-well plate, 5 µL of this solution was then mixed with 95 µL of 0.13 mg/mL *o*-
467 cresolphthalein complexone (oCPC) in 0.1 M CAPS, pH 10. The absorbance at 575 nm was measured on
468 a Tecan Infinite M200 pro microplate reader and quantified on the basis of a standard $CaCl_2$ curve (Fig.
469 S4c).

470 Preparation of protein-free lipid nanodiscs

471 Preparartion of protein-free lipid nanodiscs was carried out as described by Smith *et al.*[18] and Timcenko *et*
472 *al.*[38]. In short, dried lipids were hydrated in HBS (50 mM HEPES/NaOH (pH 7.4 unless otherwise stated)
473 and 150 mM NaCl) to 10 mM final concentration for the tested lipid mixtures: 1-palmitoyl-2-oleoyl-*sn*-
474 glycero-3-phosphocholine (POPC); soy polar lipid extract (Soy PLE); *E. coli* polar lipid extract (*E. coli*
475 PLEx), which were mixed with 0.12 mM fluorescent 1,2-dioleoyl-*sn*-glycero-3-phosphoethanolamine-N-
476 (lissamine rhodamine B sulfonyl) (LissRhod PE). All lipids were purchased from Avanti Polar Lipids Plc.
477 Empty fluorescent nanodiscs were then prepared by mixing 1% MAASTY copolymer with 1 mM total
478 lipids (small unilameller vesicles (SUVs) composed of 2% LissRhod PE and 98% chosen lipid mixture)

479 in HBS with or without specified $CaCl_2$ or $MgCl_2$ concentrations in a 50 µL total volume. The mixture
480 was incubated on rotation for 2 h at 4 °C, followed by ultracentrifugation at 113,700 xg for 15 min at 4 °C
481 to remove insoluble material. The lipid nanodisc mixture was filtered through a 0.22 µm spin-filter before
482 injection onto a Superose 6 Increase 5/150 GL column (Cytiva) equilibrated in HBS at 4 °C. The eluent
483 was detected by a Shimadzu (Shimadzu Europa GmbH) liquid chromatography system equipped with an
484 autosampler (SIL-40), a fluorometer (RF-20A), and a PDA detector (SPD-M40). LissRhod PE was
485 detected with an excitation wavelength of 554 nm and emission of 576 nm. Each sample was injected at
486 least twice to check reproducibility.

487 Membrane protein expression

488 All tested membrane proteins were expressed in HEK293 suspension cells using the baculovirus
489 expression system and a modified version of the BacMam vector pEG[69]. HEK293 cells were cultured at
490 37 °C, 8 % CO_2. rSERCA1a (rabbit sarcoendoplasmic reticulum Ca^{2+} ATPase) with a C-terminal eGFP-
491 StrepII tag and cASIC1 (chicken acid-sensing ion channel 1) with an N-terminal His_8-eGFP tag were
492 expressed in HEK293S GnTI$^-$ cells (ATCC) and enhanced with 10 mM sodium butyrate (NaBu) 10 h
493 post-transduction. Cells were harvested 72 h and 48 h post-transduction, respectively. hKCNK18 (human
494 potassium channel subfamily K member 18) with an N-terminal StrepII-eGFP tag was expressed in
495 FreeStyle™ 293-F (HEK293F) cells (Thermo Fisher Scientific, TFS) and enhanced with 10 mM NaBu 10
496 h post transduction and harvested 48 h post-transduction. hTRPM4 (human transient receptor potential
497 melastatin type 4) fused with an N-terminal StrepTagII-eGFP tag was expressed in HEK293F cells and
498 enhanced with 10 mM NaBu 24 h post-transduction and collected 48 h post-transduction as described in
499 Autzen *et al.*[45].

500 FSEC of membrane proteins in copolymer lipid nanodiscs

501 HEK293 cell pellets were resuspended in HBS supplemented with cOmplete™ EDTA-free protease
502 inhibitor cocktail (Sigma-Aldrich) at 50 µL/~1 million cells/condition. 50 µL of the cell suspension was

503 mixed with 50 µL 4% (w/v) polymer in HBS for a final concentration of 2% (w/v), briefly sonicated with
504 a probe sonicator and incubated on a rolling table for 2-4 h at 4 °C. Large aggregates were removed from
505 the suspension by ultracentrifugation at 113,700 xg for 15 min and the supernatant containing protein-
506 filled lipid nanodiscs was filtered with a 0.22 µm spin filter before being loaded onto a Superose 6
507 Increase 5/150 GL column (Cytiva) equilibrated with HBS at 4 °C. The eluent was detected by a
508 Shimadzu (Shimadzu Europa GmbH) liquid chromatography system equipped with an autosampler (SIL-
509 40), a fluorometer (RF-20A), and a PDA detector (SPD-M40). eGFP was detected with an excitation
510 wavelength of 488 nm and emission of 507 nm. Each sample was injected at least twice to check
511 reproducibility.

512 Purification of hTRPM4 in MAASTY$_{7.1}$-50 lipid nanodiscs

513 Harvested hTRPM4-expressing HEK293F cell pellets were resuspended in HBS supplemented with
514 Sigmafast™ EDTA-free protease inhibitor cocktail (Sigma-Aldrich) and lyzed by pressure homogenizer
515 (Avestin Emulsiflex) with 3 passes at 1500 psi. Lysates were centrifuged at 26,000 xg for 25 min (Sorvall
516 RC 5B Plus) followed by membrane isolation through ultracentrifugation at 55,000 pm for 1 h (Beckman,
517 Type 70 Ti Rotor). Membranes were resuspended in HBS by mortar and pestle at 20 mL/g and snap-
518 frozen in LN_2 before storage at -80 °C until further use. Purification of hTRPM4 was carried out similarly
519 to the procedure described in Smith *et al.*[18]. In short, isolated membranes were solubilized in 2% (w/v)
520 MAASTY$_{7.1}$-50 (1 g/40 mL) for 2 h at 4 °C on a rolling table and insoluble fragments separated by
521 centrifugation at 30,000 xg for 30 min. The supernatant was incubated overnight at 4 °C with StrepTactin
522 beads (Cytiva) in HBS with 250 mM L-Arginine-HCl. Under gravity flow, the beads were washed in
523 HBS with 250 mM L-Arginine-HCl, then the protein eluted upon addition of 5 mM desthiobiotin.
524 Protein-positive fractions were pooled and spin-concentrated to less than 500 µL. TEV protease was
525 added at a 1:5 molar ratio (TEV:hTRPM4) and incubated overnight at 4 °C to remove the fusion tag. The
526 sample was filtered with a 0.22 µm spin filter unit before loading onto a Superose 6 Increase 10/300 GL
527 column (Cytiva) equilibrated with HBS on an AKTA Pure Pro-¨ tein Purification System (Cytiva). Peak

528 fractions were pooled and spin-concentrated (determined by NanoDrop UV-vis spectrophotometer 280
529 nm, 1 mg = 1 Abs) before assessment by either single-particle cryo-EM, MALDI-TOF MS or lipidomics
530 analysis. Eluted fractions from size-exclusion chromatography were assessed for purity by SDS-PAGE
531 (Fig. S8).

532 MALDI-TOF MS

533 Purified hTRPM4 in $MAASTY_{7.1}$-50 nanodiscs (0.1 mL) were extracted with a 9:1 $CHCl_3$/MeOH
534 solution (0.3 mL). The extract was mixed with 2,5-dihydroxybenzoic acid (DHB) (20 mg/mL) in 9:1
535 $CHCl_3$/MeOH matrix to a final concentration of 10 mg/mL of DHB. Mass spectra were recorded on a
536 Bruker AutoflexTM MALDI-TOF MS Spectrometer.

537 Lipidomics analysis

538 Purified hTRPM4 in $MAASTY_{7.1}$-50 lipid nanodiscs (~2 mg/mL) was mixed with trypsin (Promega,
539 sequencing grade) in a 1:25 molar ratio in 100 mM ammonium bicarbonate pH 8, and digested overnight
540 at 37 °C. Lyophilized mix of peptides and lipids was dissolved in 68% solution A (acetonitrile:H_2O
541 60:40, 10 mM ammonium formate and 0.1% formic acid) and 32% solvent B (isopropanol:acetonitrile
542 90:10, 10 mM ammonium formate and 0.1% formic acid) for analysis by reverse-phase liquid
543 chromatography tandem MS (RP LC–MS/MS). RP LC–MS/MS was performed using a Dionex UltiMate
544 3000 RSLC Nano system coupled to an Orbitrap Eclipse Tribrid Mass Spectrometer (TFS). The
545 peptide/lipid mixture was loaded onto a C18 column (Acclaim PepMap 100, C18, 75 µm x 15 cm,
546 Thermo Scientific™) at a flow rate of 300 nL min^{-1}. After 10 min, solvent B was ramped to 65% over 1
547 min, then 80% over 6 min, before being held at 80% for 10 min, then ramped to 99% over 6 min and held
548 for 7 min for a total run of 45 min.

549 The mass spectrometer was set with a spray voltage of 2.4 kV and capillary temperature of 320 °C.
550 Analysis was done in negative mode, as a data-dependant acquisition. Survey full-scan MS spectra were

551 acquired on the Orbitrap (m/z 300–2,000) with a resolution of 120,000. Higher-energy Collision-induced
552 Dissociation (HCD) fragmentation was done for the N most intense ions within 3 second cycle time, with
553 max injection time of 50 ms and normalized collision energy of 25%, followed by a ramp to to 30%. The
554 MS/MS analysis was done in the Orbitrap, at 15,000 resolution and the first mass at 75 m/z, max injection
555 time of 50 ms and isolation window of 1.5 m/z.

556 Lipid identification was performed using LipiDex software (v.1.1) with the LipiDex HCD _ Formic
557 library. The MS and MS/MS search tolerances were set to 0.01 m/z. List of potential adducts was
558 manually curated, whereby a singly charged ion with formate adduct ($[M + HCOO]^-$) was added to the
559 list, as well as singly charged deprotonated ion ($[M-H]^-$). Chromatogram integration and lipid
560 quantification was carried out using MZmine (v.2.54), adapting the integrated LipiDex-MZmine
561 workflow proposed by Hutchins *et al.*[70].

562 MP analysis

563 MP analyses were performed with a Refeyn Two^{MP} mass photometer (Refeyn Ltd). Data was acquired
564 using AcquireMP (Refeyn Ltd, version 2.3). The instrument was calibrated using in-house prepared
565 protein standards of Dynamin ΔPRD, which forms oligomeric configurations of the following masses: 90,
566 180, 360 kDa[71]. Strict linear response for calibration curves was observed and extrapolated with high
567 confidence. Purified hTRPM4 in MAASTY$_{7.1}$-50 lipid nanodiscs in its isolation buffer from SEC was
568 diluted in phosphate-buffered saline (PBS) immediately before the MP acquisition to a final concentration
569 of 50-300 nM, depending on the run. The focal plane was located using 15 μL PBS, immediately after,
570 the protein was mixed into the PBS droplet, diluting it 4 times in the process. The acquisitions were
571 collected in the large field of view mode for 60 sec. The raw data were processed and manually curated
572 using DiscoverMP (Refeyn Ltd, version 2.3) to calculate the histograms of the binding events for mass
573 determination and integrate them for quantification of different mass species. Factory-set video
574 processing settings were used for mass histogram calculations.

575 ## Determination of the hTRPM4-MAASTY nanodisc composition

576 Harvested HEK293F cell membranes expressing hTRPM4 were solubilized with 1% (w/v) $MAASTY_{7.1}$-
577 50_{ttc} and purified as described above. Final protein concentration was determined through Bradford assay
578 against a BSA standard curve. A calculated 10 µg purified hTRPM4 was injected onto a Superose 6
579 Increase 5/150 gel filtration column and measured for absorbance at 280 nm (protein) and 310 nm (ttc).
580 Specified concentrations of $MAASTY_{7.1}$-50_{ttc} copolymer were injected onto a Superose 6 Increase 5/150
581 gel filtration column and measured at 310 nm absorbance to construct a standard curve of ttc
582 concentration. Total $MAASTY_{7.1}$-50_{ttc} per mole hTRPM4 was then calculated using the peak 310 nm
583 absorbance values. Remaining lipid content was calculated using the MP analysis, which determined the
584 molecular weight per particle, the molecular weight of hTRPM4, and the molecular weight of the
585 encasing copolymers.

586 ## Purification of hTRPM4 in MSP2N2 lipid nanodiscs

587 hTRPM4 was purified in n-Dodecyl-beta-D-maltoside (DDM) and cholesteryl hemisuccinate (CHS) and
588 reconstituted in MSP2N2 nanodiscs as described in Autzen *et al.*[45]. The final concentration of the sample
589 was 2.2 mg/mL to which $CaCl_2$ was added to a final of 5 mM just before vitrification.

590 ## Negative stain EM of hTRPM4 and HEK293F membranes

591 EM grids of negatively stained hTRPM4-MAASTY nanodiscs or MAASTY solubilized HEK293
592 membranes were prepared by applying 3 µL of sample (0.06-0.3 mg/mL for hTRPM4-MAASTY,
593 determined by Implen UV-vis NanoPhotometer 280 nm, 1 mg = 1 Abs) to a 400-mesh copper grid
594 covered with continuous carbon film and stained with 2 % (w/v) uranyl acetate. Negative-stain EM grids
595 were imaged on a CM100 microscope (Philips) operated at 100 kV and equipped with an Olympus Veleta
596 camera. Images were recorded at a nominal magnification of 135,000x, corresponding to a pixel size of
597 3.8 Å.

598 ## Cryo-EM sample preparation and data collection

599 Cryo-EM grids were prepared by adding 4 µL of ~1.4 mg/mL purified hTRPM4-MAASTY or 2.2
600 mg/mL hTRPM4-MSP2N2 in lipid nanodiscs to glow-discharged Quantifoil R1.2/1.3 300-mesh Au holey
601 carbon grids (Quantifoil, Micro Tools GmbH). The grids were blotted with Whatman Grade 1 filter paper
602 for 3 s at 4 °C and 100% humidity, then plunge-frozen into liquid ethane using a by Vitrobot™ Mark IV
603 (TFS). Datasets were collected on a Titan Krios G2cA cryo-transmission electron microscope equipped
604 with a Thermo Scientific™ Selectris X imaging filter and a Falcon4i detector. Grid squares were
605 manually selected and movies were recorded in counting mode using EPU (TFS) at a nominal
606 magnification of 165kx, corresponding to a physical pixel size of 0.725 Å. Data were collected with a
607 defocus range of 0.8 to 2.5 µm and a total electron dose of 52 $e^-/Å^2$. Images were saved as Electron Event
608 Recordings (EER). Details on data collections are included in Table S1.

609 ## Image processing

610 Pre-processing of both nanodisc samples was performed in cryoSPARC live v4.4.0 for initial assessment
611 of sample quality during which patch-based motion correction was used for aligning EM movie stacks,
612 and applying dose-dependent weighting[72]. Further processing was performed using a combination of
613 cryoSPARC v4.4.0[72] and Relion 5.0[73].

614 For hTRPM4 in $MAASTY_{7.1}$-50 nanodiscs, a total of 6308 movies at 0.749 Å/pixel were collected. This
615 predetermined pixel size was later corrected to 0.725 Å/pixel in post-processing following an accurate
616 determination of pixel size, better reflecting the detector specifications. In cryoSPARC v4.4.0, motion
617 corrected micrographs were patch-based CTF corrected before curating to 6070 micrographs. Particle
618 picking was first carried out using blob picker, from which two rounds of 2D classifications identified
619 classes used as templates for template-based picking. These 1,306,897 particles underwent three rounds of
620 2D classification leaving 126,417 particles remaining. An *ab initio* model was generated and classified
621 using heterogeneous refinement. The best class of 87,697 particles was refined further by non-uniform

622 refinement, resulting in a reconstruction with an estimated resolution of 3.23 Å. Due to lower local
623 resolution in the cytosolic regions, we re-extracted the refined particles in Relion 5.0, after particle stack
624 conversion by pyEM[74], from micrographs motion-corrected using the CPU-based implementation of
625 MotionCor2[75]. The particles underwent refinement applying C4 symmetry and BLUSH regularization[76]
626 resulting in a 3.46 Å resolution reconstruction following post-processing with a soft mask. Details on
627 image processing and final reconstructions of hTRPM4 in MAASTY nanodiscs are included in Fig. S10,
628 S11, and Table S1.

629 For this study, we solved the hTRPM4-MSP2N2 structure from cryo-EM data collected on gold grids in
630 contrast to the structures from Autzen *et al.*[45] which were solved from data collected on copper grids. For
631 hTRPM4 in MSP2N2 nanodiscs, a total of 7,945 EER format movies at 0.725 Å/pixel were collected and
632 imported into Relion 5.0[73]. Movies were motion corrected with the CPU-based implementation of
633 MotionCor2 using an EER fractionation of 40, and dividing whole frames into 5 × 5 patches[75].
634 Micrographs were CTF corrected with ctffind 4.1[77], manually curated and micrographs with resolution
635 lower than 6 Å were discarded, resulting in 7627 micrographs to pick particles from. Particle picking was
636 first carried out using a Laplacian-of-Gaussian (LoG) filter from which a round of 2D classifications
637 helped identify classes that were used as templates for template-based picking. 1,104,004 particles were
638 subjected to a single round of 2D classification (EM algorithm, 25 iterations) resulting in 255,586 good
639 looking particles. These particles were used for determination of an *ab initio* model and subjected to 3D
640 classification. The particles belonging to the two best looking classes were combined and refined in 3D
641 with BLUSH regularization[76] resulting in a reconstruction with an estimated resolution of 3.8 Å. Details
642 on image processing and final reconstructions of hTRPM4 in MSP2N2 nanodiscs are included in Fig.
643 S13, Fig. S12 and Table S1.

644 Model building and refinement

645 Atomic models for hTRPM4 in MAASTY$_{7.1}$-50 and MSP2N2 were built using Coot v0.9.8.94[78] using the
646 hTRPM4-MSP2N2 Ca^{2+} model 6BQV[45] as the initial model. Residues missing from the reconstructions
647 were not modeled. In the case of the MAASTY$_{7.1}$-50 structure, this included MHR1-3, in addition to
648 residues predicted to be unstructured which were missing from both structures. Table S1 provides an
649 overview of the residues included in the final, refined models in addition to their refinement and
650 validation statistics by Phenix and MolProbity (within Phenix version 1.21.1-5286)[79,80]. Both models were
651 subjected to real-space refinement using Phenix v1.21.1-5286 with a general restaints setup. As cross-
652 validations, the final models were refined against the finalized maps generated by Relion 5.0 (Fig. S10;
653 Fig. S13). The program HOLE[81] was used to calculate the pore profiles shown in Fig.3e. UCSF
654 ChimeraX was used to prepare figures[82].

655 Data Availability

656 The reconstructed maps are available from the EMDB under access codes EMD-52611 (hTRPM4 in
657 MAASTY) and EMD-????? (hTRPM4 in MSP2N2). The atomic models are available from the PDB
658 under access codes PDB 9I3R (hTRPM4 in MAASTY) and ???? (hTRPM4 in MSP2N2). The raw cryo-
659 EM movies data used in our study are available under access codes EMPIAR-????? and EMPIAR-?????.
660 Plasmids and other data that support the findings of this study are available from the corresponding
661 authors upon reasonable request. Source data are provided in this paper.

662 Code Availability

663 The code used for data analysis in this study was implemented using Python 3.10.6. All scripts and
664 computational workflows necessary to reproduce the results are available upon reasonable request from
665 the corresponding authors.

666 References

667 1. Santos, R., Ursu, O., Gaulton, A., Bento, A. P., Donadi, R. S., Bologa, C. G., Karlsson, A., Al-Lazikani,
668 B., Hersey, A., Oprea, T. I. & Overington, J. P. A comprehensive map of molecular drug targets.
669 *Nat Rev Drug Discov* **16,** 19–34 (2016).

670 2. Cheng, Y. Single-particle cryo-EM—How did it get here and where will it go. *Science* **361,** 876–
671 880 (2018).

672 3. Autzen, H. E., Julius, D. & Cheng, Y. Membrane mimetic systems in CryoEM: keeping membrane
673 proteins in their native environment. *Curr Opin Struct Biol* **58,** 259–268 (2019).

674 4. Denisov, I. G. & Sligar, S. G. Nanodiscs for structural and functional studies of membrane
675 proteins. *Nat Struct Mol Biol* **23,** 481–486 (2016).

676 5. Frauenfeld, J., Löving, R., Armache, J. P., Sonnen, A. F. P., Guettou, F., Moberg, P., Zhu, L.,
677 Jegerschöld, C., Flayhan, A., Briggs, J. A. G., Garoff, H., Löw, C., Cheng, Y. & Nordlund, P. A
678 saposin-lipoprotein nanoparticle system for membrane proteins. *Nat Methods* **13,** 345–351
679 (2016).

680 6. Duan, J., Li, J., Chen, G.-L., Ge, Y., Liu, J., Xie, K., Peng, X., Zhou, W., Zhong, J., Zhang, Y., Xu, J.,
681 Xue, C., Liang, B., Zhu, L., Liu, W., Zhang, C., Tian, X.-L., Wang, J., Clapham, D. E., Zeng, B., Li, Z. &
682 Zhang, J. Cryo-EM structure of TRPC5 at 2.8-Å resolution reveals unique and conserved structural
683 elements essential for channel function. *Sci Adv* **5,** 7935–7959 (2019).

684 7. Bolla, J. R., Corey, R. A., Sahin, C., Gault, J., Hummer, A., Hopper, J. T. S., Lane, D. P., Drew, D.,
685 Allison, T. M., Stansfeld, P. J., Robinson, C. V. & Landreh, M. A Mass-Spectrometry-Based
686 Approach to Distinguish Annular and Specific Lipid Binding to Membrane Proteins. *Angewandte*
687 *Chemie* **132,** 3551–3556 (2020).

688 8. Bechara, C. & Robinson, C. V. Different modes of lipid binding to membrane proteins probed by
689 mass spectrometry. *J Am Chem Soc* **137,** 5240–5247 (2015).

690 9. Dörr, J. M., Koorengevel, M. C., Schäfer, M., Prokofyev, A. V., Scheidelaar, S., van der Cruijsen, E.
691 A. W., Dafforn, T. R., Baldus, M. & Killian, J. A. Detergent-free isolation, characterization, and
692 functional reconstitution of a tetrameric K+ channel: The power of native nanodiscs. *Proceedings*
693 *of the National Academy of Sciences* **111,** 18607–18612 (2014).

694 10. Gulati, S., Jamshad, M., Knowles, T. J., Morrison, K. A., Downing, R., Cant, N., Collins, R.,
695 Koenderink, J. B., Ford, R. C., Overduin, M., Kerr, I. D., Dafforn, T. R. & Rothnie, A. J. Detergent-
696 free purification of ABC (ATP-binding-cassette) transporters. *Biochemical Journal* **461,** 269–278
697 (2014).

698 11. Orwick-Rydmark, M., Lovett, J. E., Graziadei, A., Lindholm, L., Hicks, M. R. & Watts, A. Detergent-
699 free incorporation of a seven-transmembrane receptor protein into nanosized bilayer lipodisq
700 particles for functional and biophysical studies. *Nano Lett* **12,** 4687–4692 (2012).

701 12. Knowles, T. J., Finka, R., Smith, C., Lin, Y. P., Dafforn, T. & Overduin, M. Membrane proteins
702 solubilized intact in lipid containing nanoparticles bounded by styrene maleic acid copolymer. *J*
703 *Am Chem Soc* **131,** 7484–7485 (2009).

704 13. Krishnarjuna, B. & Ramamoorthy, A. Detergent-Free Isolation of Membrane Proteins and
705 Strategies to Study Them in a Near-Native Membrane Environment. *Biomolecules* **12,** (2022).

706 14. Brown, C. J., Trieber, C. & Overduin, M. Structural biology of endogenous membrane protein
707 assemblies in native nanodiscs. *Curr Opin Struct Biol* **69,** 70–77 (2021).

15. Parmar, M., Rawson, S., Scarff, C. A., Goldman, A., Dafforn, T. R., Muench, S. P. & Postis, V. L. G. Using a SMALP platform to determine a sub-nm single particle cryo-EM membrane protein structure. *Biochimica et Biophysica Acta (BBA) - Biomembranes* **1860,** 378–383 (2018).

16. Sun, C., Benlekbir, S., Venkatakrishnan, P., Wang, Y., Hong, S., Hosler, J., Tajkhorshid, E., Rubinstein, J. L. & Gennis, R. B. Structure of the alternative complex III in a supercomplex with cytochrome oxidase. *Nature* **557,** 123–126 (2018).

17. Swainsbury, D. J. K., Hawkings, F. R., Martin, E. C., Musiał, S., Salisbury, J. H., Jackson, P. J., Farmer, D. A., Johnson, M. P., Siebert, C. A., Hitchcock, A. & Hunter, C. N. Cryo-EM structure of the four-subunit *Rhodobacter sphaeroides* cytochrome bc_1 complex in styrene maleic acid nanodiscs. *Proceedings of the National Academy of Sciences* **120,** (2023).

18. Smith, A. A. A., Autzen, H. E., Faust, B., Mann, J. L., Muir, B. W., Howard, S., Postma, A., Spakowitz, A. J., Cheng, Y. & Appel, E. A. Lipid Nanodiscs via Ordered Copolymers. *Chem* **6,** 2782–2795 (2020).

19. Yoder, N. & Gouaux, E. The His-Gly motif of acid-sensing ion channels resides in a reentrant 'loop' implicated in gating and ion selectivity. *Elife* **9,** 1–18 (2020).

20. Harwood, C. R., Sykes, D. A., Hoare, B. L., Heydenreich, F. M., Uddin, R., Poyner, D. R., Briddon, S. J. & Veprintsev, D. B. Functional solubilization of the β2-adrenoceptor using diisobutylene maleic acid. *iScience* **24,** 103362 (2021).

21. Ekundayo, B., Arullampalam, P., Gerber, C. E., Hämmerli, A.-F., Guichard, S., Boukenna, M., Ross-Kaschitza, D., Lochner, M., Rougier, J.-S., Stahlberg, H., Abriel, H. & Ni, D. Identification of a binding site for small molecule inhibitors targeting human TRPM4. *Nat Commun* **16,** 833 (2025).

22. Adair, B. D., Xiong, J.-P., Yeager, M. & Arnaout, M. A. Cryo-EM structures of full-length integrin αIIbβ3 in native lipids. *Nat Commun* **14,** 4168 (2023).

23. Di Mauro, G. M., La Rosa, C., Condorelli, M. & Ramamoorthy, A. Benchmarks of SMA-Copolymer Derivatives and Nanodisc Integrity. *Langmuir* **37,** 3113–3121 (2021).

24. Catalano, C., Ben-Hail, D., Qiu, W., Blount, P., des Georges, A. & Guo, Y. Cryo-em structure of mechanosensitive channel ynai using sma2000: Challenges and opportunities. *Membranes (Basel)* **11,** (2021).

25. Sinha, S., Kumar, S., Singh, K., Umam, F., Agrawal, V., Aggarwal, A. & Imperiali, B. Immunochemical characterisation of styrene maleic acid lipid particles prepared from Mycobacterium tuberculosis plasma membrane. *PLoS One* **18,** (2023).

26. Dörr, J. M., Scheidelaar, S., Koorengevel, M. C., Dominguez, J. J., Schäfer, M., van Walree, C. A. & Killian, J. A. The styrene–maleic acid copolymer: a versatile tool in membrane research. *European Biophysics Journal* **45,** 3–21 (2016).

27. Kopf, A. H., Dörr, J. M., Koorengevel, M. C., Antoniciello, F., Jahn, H. & Killian, J. A. Factors influencing the solubilization of membrane proteins from Escherichia coli membranes by styrene–maleic acid copolymers. *Biochim Biophys Acta Biomembr* **1862,** (2020).

745 28. Krishnarjuna, B., Ravula, T. & Ramamoorthy, A. Detergent-free extraction, reconstitution and
746 characterization of membrane-anchored cytochrome-b5 in native lipids. *Chemical*
747 *Communications* **56,** 6511–6514 (2020).

748 29. Oluwole, A. O., Danielczak, B., Meister, A., Babalola, J. O., Vargas, C. & Keller, S. Solubilization of
749 Membrane Proteins into Functional Lipid-Bilayer Nanodiscs Using a Diisobutylene/Maleic Acid
750 Copolymer. *Angewandte Chemie - International Edition* **56,** 1919–1924 (2017).

751 30. Yasuhara, K., Arakida, J., Ravula, T., Ramadugu, S. K., Sahoo, B., Kikuchi, J. I. & Ramamoorthy, A.
752 Spontaneous Lipid Nanodisc Fomation by Amphiphilic Polymethacrylate Copolymers. *J Am Chem*
753 *Soc* **139,** 18657–18663 (2017).

754 31. Esmaili, M., Brown, C. J., Shaykhutdinov, R., Acevedo-Morantes, C., Wang, Y. L., Wille, H.,
755 Gandour, R. D., Turner, S. R. & Overduin, M. Homogeneous nanodiscs of native membranes
756 formed by stilbene-maleic-acid copolymers. *Nanoscale* **12,** 16705–16709 (2020).

757 32. Ravula, T. & Ramamoorthy, A. Synthesis, Characterization, and Nanodisc Formation of Non-ionic
758 Polymers**. *Angewandte Chemie International Edition* **60,** 16885–16888 (2021).

759 33. Burridge, K. M., Harding, B. D., Sahu, I. D., Kearns, M. M., Stowe, R. B., Dolan, M. T., Edelmann, R.
760 E., Dabney-Smith, C., Page, R. C., Konkolewicz, D. & Lorigan, G. A. Simple Derivatization of RAFT-
761 Synthesized Styrene-Maleic Anhydride Copolymers for Lipid Disk Formulations.
762 *Biomacromolecules* **21,** 1274–1284 (2020).

763 34. Esmaili, M., Acevedo-Morantes, C., Wille, H. & Overduin, M. The effect of hydrophobic alkyl
764 sidechains on size and solution behaviors of nanodiscs formed by alternating styrene maleamic
765 copolymer. *Biochimica et Biophysica Acta (BBA) - Biomembranes* **1862,** 183360 (2020).

766 35. Ravula, T., Hardin, N. Z., Ramadugu, S. K. & Ramamoorthy, A. pH Tunable and Divalent Metal Ion
767 Tolerant Polymer Lipid Nanodiscs. *Langmuir* **33,** 10655–10662 (2017).

768 36. Fiori, M. C., Jiang, Y., Altenberg, G. A. & Liang, H. Polymer-encased nanodiscs with improved
769 buffer compatibility. *Sci Rep* **7,** 1–10 (2017).

770 37. Moad, G., Rizzardo, E. & Thang, S. H. Living Radical Polymerization by the RAFT Process – A Third
771 Update. *Aust J Chem* **65,** 985 (2012).

772 38. Timcenko, M., Autzen, A. A. A. & Autzen, H. E. Characterization of Divalent Cation Interactions
773 with AASTY Nanodiscs. *ACS Appl Polym Mater* **4,** 1071–1083 (2022).

774 39. Sahloul, N. & Penlidis, A. Styrene/Methacrylic Acid Monomer Reactivity Ratio Estimation in Bulk
775 and Solution at High Temperatures. *Polym Plast Technol Eng* **44,** 771–782 (2005).

776 40. Smith, A. A. A., Hall, A., Wu, V. & Xu, T. Practical Prediction of Heteropolymer Composition and
777 Drift. *ACS Macro Lett* **8,** 36–40 (2019).

778 41. Harrisson, S., Ercole, F. & Muir, B. W. Living spontaneous gradient copolymers of acrylic acid and
779 styrene: One-pot synthesis of pH-responsive amphiphiles. *Polym Chem* **1,** 326–332 (2010).

780 42. Ravula, T., Dai, X. & Ramamoorthy, A. Solid-State NMR Study to Probe the Effects of Divalent
781 Metal Ions (Ca2+ and Mg2+) on the Magnetic Alignment of Polymer-Based Lipid Nanodiscs.
782 *Langmuir* **37,** 7780–7788 (2021).

783 43. Ilka, M., Jacobs, G., Kecskes, M., Menigoz, A., Philippaert, K. & Vennekens, R. *Mammalian*
784 *Transient Receptor Potential (TRP) Cation Channels*. *Handb Exp Pharmacol* **1,** 461-487 (2014).

785 44. Winkler, P. A., Huang, Y., Sun, W., Du, J. & Lü, W. Electron cryo-microscopy structure of a human
786 TRPM4 channel. *Nature* **552,** 200–204 (2017).

787 45. Autzen, H. E., Myasnikov, A. G., Campbell, M. G., Asarnow, D., Julius, D. & Cheng, Y. Structure of
788 the human TRPM4 ion channel in a lipid nanodisc. *Science* **359,** 228–232 (2018).

789 46. Duan, J., Li, Z., Li, J., Santa-Cruz, A., Sanchez-Martinez, S., Zhang, J. & Clapham, D. E. Structure of
790 full-length human TRPM4. *Proceedings of the National Academy of Sciences* **115,** 2377–2382
791 (2018).

792 47. Hu, J., Park, S. J., Walter, T., Orozco, I. J., O'Dea, G., Ye, X., Du, J. & Lü, W. Physiological
793 temperature drives TRPM4 ligand recognition and gating. *Nature* **630,** 509–515 (2024).

794 48. Gao, Y., Cao, E., Julius, D. & Cheng, Y. TRPV1 structures in nanodiscs reveal mechanisms of ligand
795 and lipid action. *Nature* **534,** 347–351 (2016).

796 49. Tascón, I., Sousa, J. S., Corey, R. A., Mills, D. J., Griwatz, D., Aumüller, N., Mikusevic, V., Stansfeld,
797 P. J., Vonck, J. & Hänelt, I. Structural basis of proton-coupled potassium transport in the KUP
798 family. *Nat Commun* **11,** 626 (2020).

799 50. Deng, Y., Kashtoh, H., Wang, Q., Zhen, G., Li, Q., Tang, L., Gao, H., Zhang, C., Qin, L., Su, M., Li, F.,
800 Huang, X., Wang, Y., Xie, Q., Clarke, O. B., Hendrickson, W. A. & Chen, Y. Structure and activity of
801 SLAC1 channels for stomatal signaling in leaves. *Proceedings of the National Academy of Sciences*
802 **118,** (2021).

803 51. Hasselbach, W. The sarcoplasmic calcium pump. *Current Topics in Chemistry Biochemistry* **78,** 1–
804 56 (2006).

805 52. Schreiber, J. A., Düfer, M. & Seebohm, G. The Special One: Architecture, Physiology and
806 Pharmacology of the TRESK Channel. *Cellular Physiology and Biochemistry* **56,** 663–684 (2022).

807 53. Rook, M. L., Musgaard, M. & MacLean, D. M. Coupling structure with function in acid-sensing ion
808 channels: challenges in pursuit of proton sensors. *Journal of Physiology* **599,** 417–430 (2021).

809 54. Dominguez Pardo, J. J., Dörr, J. M., Iyer, A., Cox, R. C., Scheidelaar, S., Koorengevel, M. C.,
810 Subramaniam, V. & Killian, J. A. Solubilization of lipids and lipid phases by the styrene–maleic acid
811 copolymer. *European Biophysics Journal* **46,** 91–101 (2017).

812 55. Scheidelaar, S., Koorengevel, M. C., Pardo, J. D., Meeldijk, J. D., Breukink, E. & Killian, J. A.
813 Molecular Model for the solubilization of membranes into nanodisks by styrene maleic acid
814 copolymers. *Biophys J* **108,** 279–290 (2015).

815 56. Voskoboynikova, N., Margheritis, E. G., Kodde, F., Rademacher, M., Schowe, M., Budke-
816 Gieseking, A., Psathaki, O. E., Steinhoff, H. J. & Cosentino, K. Evaluation of DIBMA nanoparticles

817 of variable size and anionic lipid content as tools for the structural and functional study of
818 membrane proteins. *Biochim Biophys Acta Biomembr* **1863,** (2021).

819 57. Kopf, A. H., Lijding, O., Elenbaas, B. O. W., Koorengevel, M. C., Dobruchowska, J. M., Van Walree,
820 C. A. & Killian, J. A. Synthesis and Evaluation of a Library of Alternating Amphipathic Copolymers
821 to Solubilize and Study Membrane Proteins. *Biomacromolecules* **23,** 743–759 (2022).

822 58. Smith, A. A. A., Autzen, H. E., Laursen, T., Wu, V., Yen, M., Hall, A., Hansen, S. D., Cheng, Y. & Xu,
823 T. Controlling Styrene Maleic Acid Lipid Particles through RAFT. *Biomacromolecules* **18,** 3706–
824 3713 (2017).

825 59. Kamilar, E., Bariwal, J., Zheng, W., Ma, H. & Liang, H. SMALPs Are Not Simply Nanodiscs: The
826 Polymer-to-Lipid Ratios of Fractionated SMALPs Underline Their Heterogeneous Nature.
827 *Biomacromolecules* **24,** 1819–1838 (2023).

828 60. Cunningham, R. D., Kopf, A. H., Elenbaas, B. O. W., Staal, B. B. P., Pfukwa, R., Killian, J. A. &
829 Klumperman, B. Iterative RAFT-Mediated Copolymerization of Styrene and Maleic Anhydride
830 toward Sequence- And Length-Controlled Copolymers and Their Applications for Solubilizing Lipid
831 Membranes. *Biomacromolecules* **21,** 3287–3300 (2020).

832 61. van Meer, G., Voelker, D. R. & Feigenson, G. W. Membrane lipids: where they are and how they
833 behave. *Nat Rev Mol Cell Biol* **9,** 112–124 (2008).

834 62. Nilius, B., Mahieu, F., Prenen, J., Janssens, A., Owsianik, G., Vennekens, R. & Voets, T. The Ca2+-
835 activated cation channel TRPM4 is regulated by phosphatidylinositol 4,5-biphosphate. *EMBO*
836 *Journal* **25,** 467–478 (2006).

837 63. Zhang, Z., Okawa, H., Wang, Y. & Liman, E. R. Phosphatidylinositol 4,5-Bisphosphate rescues
838 TRPM4 channels from desensitization. *Journal of Biological Chemistry* **280,** 39185–39192 (2005).

839 64. Guo, J., She, J., Zeng, W., Chen, Q., Bai, X. C. & Jiang, Y. Structures of the calcium-activated, non-
840 selective cation channel TRPM4. *Nature* **552,** 205–209 (2017).

841 65. Koh, Y. H., Kim, S. & Roh, S. Unraveling membrane protein localization and interactions in
842 nanodiscs. *FEBS Lett* (2024).

843 66. Benítez-Angeles, M., Romero, A. E. L., Llorente, I., Hernández-Araiza, I., Vergara-Jaque, A., Real, F.
844 H., Gutiérrez Castañeda, Ó. E., Arciniega, M., Morales-Buenrostro, L. E., Torres-Quiroz, F., García-
845 Villegas, R., Tovar-Y-Romo, L. B., Liedtke, W. B., Islas, L. D. & Rosenbaum, T. Modes of action of
846 lysophospholipids as endogenous activators of the TRPV4 ion channel. *J Physiol* **601,** 1655–1673
847 (2023).

848 67. Bang, S., Yoo, S., Oh, U. & Hwang, S. W. Endogenous lipid-derived ligands for sensory TRP ion
849 channels and their pain modulation. *Arch Pharm Res* **33,** 1509–1520 (2010).

850 68. Blumstein, R., Murphy, G. J., Blumstein, A. & Watterson, A. C. An improved methylating agent for
851 poly-(methacrylic) acid: 1-methyl-3-p-tolyltriazene. *Journal of Polymer Science: Polymer Letters*
852 *Edition* **11,** 21–23 (1973).

853 69. Goehring, A., Lee, C. H., Wang, K. H., Michel, J. C., Claxton, D. P., Baconguis, I., Althoff, T., Fischer,
854 S., Garcia, K. C. & Gouaux, E. Screening and large-scale expression of membrane proteins in
855 mammalian cells for structural studies. *Nat Protoc* **9,** (2014).

856 70. Hutchins, P. D., Russell, J. D. & Coon, J. J. LipiDex: An Integrated Software Package for High-
857 Confidence Lipid Identification. *Cell Syst* **6,** 621-625.e5 (2018).

858 71. Becker, J., Peters, J. S., Crooks, I., Helmi, S., Synakewicz, M., Schuler, B. & Kukura, P. A
859 Quantitative Description for Optical Mass Measurement of Single Biomolecules. *ACS Photonics*
860 **10,** 2699–2710 (2023).

861 72. Punjani, A., Rubinstein, J. L., Fleet, D. J. & Brubaker, M. A. cryoSPARC: algorithms for rapid
862 unsupervised cryo-EM structure determination. *Nat Methods* **14,** 290–296 (2017).

863 73. Burt, A., Toader, B., Warshamanage, R., von Kügelgen, A., Pyle, E., Zivanov, J., Kimanius, D.,
864 Bharat, T. A. M. & Scheres, S. H. W. An image processing pipeline for electron cryo-tomography in
865 RELION-5. *FEBS Open Bio* **14,** 1788–1804 (2024).

866 74. Asarnow, D., Palovcak, E. & Cheng, Y. UCSF pyem v0.5. *Zenodo* (2019).

867 75. Zheng, S. Q., Palovcak, E., Armache, J.-P., Verba, K. A., Cheng, Y. & Agard, D. A. MotionCor2:
868 anisotropic correction of beam-induced motion for improved cryo-electron microscopy. *Nat*
869 *Methods* **14,** 331–332 (2017).

870 76. Kimanius, D., Jamali, K., Wilkinson, M. E., Lövestam, S., Velazhahan, V., Nakane, T. & Scheres, S.
871 H. W. Data-driven regularisation lowers the size barrier of cryo-EM structure determination.
872 *bioRxiv* (2023).

873 77. Rohou, A. & Grigorieff, N. CTFFIND4: Fast and accurate defocus estimation from electron
874 micrographs. *J Struct Biol* **192,** 216–221 (2015).

875 78. Emsley, P. & Cowtan, K. Coot: Model-building tools for molecular graphics. *Acta Crystallogr D Biol*
876 *Crystallogr* **60,** 2126–2132 (2004).

877 79. Afonine, P. V., Klaholz, B. P., Moriarty, N. W., Poon, B. K., Sobolev, O. V., Terwilliger, T. C., Adams,
878 P. D. & Urzhumtsev, A. New tools for the analysis and validation of cryo-EM maps and atomic
879 models. *Acta Crystallogr D Struct Biol* **74,** 814–840 (2018).

880 80. Williams, C. J., Headd, J. J., Moriarty, N. W., Prisant, M. G., Videau, L. L., Deis, L. N., Verma, V.,
881 Keedy, D. A., Hintze, B. J., Chen, V. B., Jain, S., Lewis, S. M., Arendall, W. B., Snoeyink, J., Adams, P.
882 D., Lovell, S. C., Richardson, J. S. & Richardson, D. C. MolProbity: More and better reference data
883 for improved all-atom structure validation. *Protein Science* **27,** 293–315 (2018).

884 81. Smart, O. S., Neduvelil, J. G., Wang, X., Wallace, B. A. & Sansom, M. S. P. HOLE: A program for the
885 analysis of the pore dimensions of ion channel structural models. *J Mol Graph* **14,** 354–360
886 (1996).

887 82. Pettersen, E. F., Goddard, T. D., Huang, C. C., Meng, E. C., Couch, G. S., Croll, T. I., Morris, J. H. &
888 Ferrin, T. E. UCSF ChimeraX: Structure visualization for researchers, educators, and developers.
889 *Protein Science* **30,** 70–82 (2021).

890

891 ## Acknowledgements

892 The authors thank senior research scientists Tillmann Hanns Pape, Nicholas Heelund Sofos and Michael
893 James Johnson for their support for cryo-EM experiments at the Core Facility for Integrated Microscopy
894 at University of Copenhagen. The authors thank members of the Autzen Group for data discussion.
895 hTRPM4 was expressed in a modified version of a BacMam vector gifted from Eric Gouaux (Addgene
896 plasmid # 160680). Subsets of the figures were created with BioRender.com.

897 ## Funding

898 H.E.A acknowledges the Novo Nordisk Foundation (NNF20OC0060692), the Carlsberg Foundation
899 (CF20-0533), and Independent Research Fund Denmark (1131-00023B) for support. A.A.A.A.
900 acknowledges Independent Research Fund Denmark (0171-00081B) for support. J.R.B. acknowledges the
901 Royal Society for the support through the University Research Fellowship grant (URF\R1\211567).

902 ## Author Contributions

903 H.E.A., and A.A.A.A. conceived the project. C.F.P., H.E.A., and A.A.A.A. designed the experimental
904 procedures. A.A.A.A., K.F.P., C.S., and N.J.B. carried out copolymer synthesis. N.J.B. carried out NMR.
905 C.F.P. carried out expression of all membrane proteins, FSEC screening of membrane proteins and
906 fluorescent lipid nanodiscs, purification and vitrification of hTRPM4 in MAASTY nanodiscs, and
907 preparation of hTRPM4 for lipidomics and MP analysis. L.P.F. purified hTRPM4 in MSP2N2 nanodiscs
908 and C.d.L vitrified the sample for cryo-EM. C.F.P. and L.P.F. performed image acquisition. C.F.P. and
909 H.E.A. performed single particle analysis. C.F.P. built atomic models. K.F.P. carried out calcium binding
910 experiments and pH sensitivity. A.A.A.A. did MALDI-TOF analysis of hTRPM4 in MAASTY. D.Z. and
911 J.R.B. carried out lipidomics analysis and MP. C.F.P., H.E.A. and A.A.A.A wrote the manuscript. C.F.P.,
912 H.E.A. and A.A.A.A. prepared figures. All authors read and reviewed the manuscript.

913 ## Competing interests

The authors declare the following competing interests: N.J.B., A.A.A.A., and H.E.A. are listed as inventors on a pending patent application describing the technology reported in this manuscript. All other authors declare no competing interests.

Inclusion and Ethics

In preparing this manuscript, we ensured equitable recognition of all contributors. This study did not involve human participants, human tissues, or animal research requiring ethical approval. The research adheres to Nature Portfolio's policies on integrity, accessibility, and reproducibility, ensuring transparency and rigor in scientific reporting.

Supplementary Information

The accompanying supplementary figures and tables are provided as a separate file.

Tables

Table 1: MAASTY copolymer characteristics. Abbreviations and symbols used: Methacrylic acid, MAA; conversion, conv.; simulated MAA fraction at given conversion, MAA frac; chemical correlation parameter, λ ($\lambda = 0$ is a perfectly random copolymer, $\lambda = -1$ is perfectly alternating); number-average molecular weight, M_n; dispersity, $Đ = M_w/M_n$, where M_w is the weight average molecular weight; acid dissociation constant, pKa. ^{1}H-NMR of all MAASTY copolymers is contained in Fig. S1. pKa was determined from the Bjerrum plot in Fig. S2.

Table 1 MAASTY copolymer characteristics.

MAASTY coolymer	Initial MAA (%)	Conv (%)	MAA frac (%)	λ	M_n kDa ^{1}H-NMR	M_n kDa SEC	Đ SEC	pKa
7.4-40	40	81	44	-0.48	7.4	5.9	1.68	8.23
7.0-45	45	73	48	-0.49	7.0	3.5	1.55	7.95
7.1-50	50	75	51	-0.49	7.1	8.9	1.99	7.75
8.2-55	55	88	55	-0.48	8.2	5.6	1.69	7.62
8.1-60	60	88	59	-0.46	8.1	6.2	1.35	7.44
8.0-65	65	88	63	-0.42	8.0	6.2	1.74	7.18

Figures

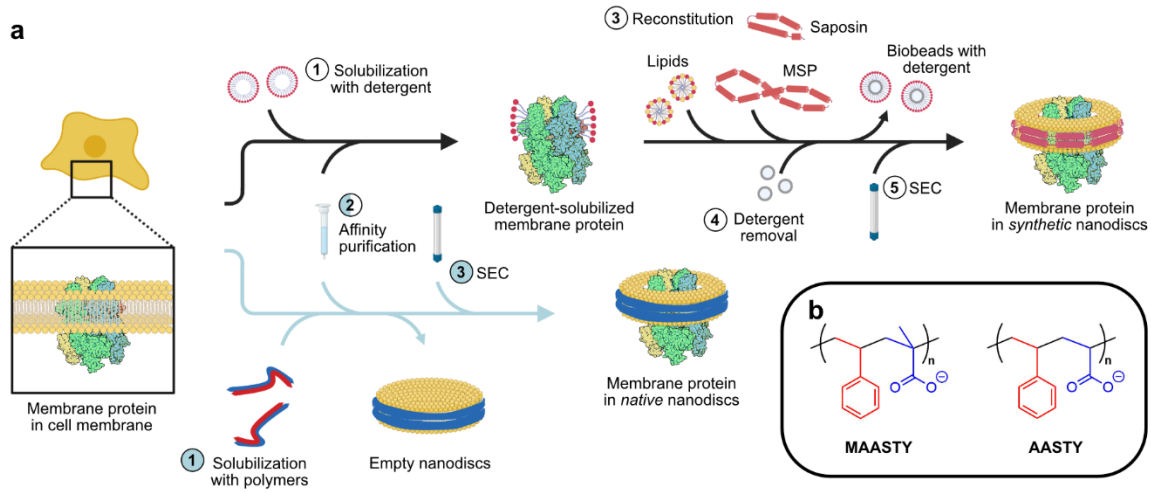

935 **Fig. 1: Overview of membrane mimetics systems and chemical composition of MAASTY**
936 **copolymers. a** Overview of the synthetic (white circles, black arrows) and native nanodisc (blue circles,
937 blue arrows) approaches. Reconstitution into synthetic nanodiscs is typically carried out using detergents
938 (steps 1–5, white circles). First, cells are treated with detergent to solubilize the proteins (step 1). The
939 detergent-solubilized, recombinant protein is then purified using affinity chromatography (step 2), then
940 reconstituted into a lipid bilayer by adding detergent-solubilized lipids and MSP or saposin (step 3)
941 during which detergent is removed with bio-beads (step 4). Finally, aggregates and/or empty discs are
942 removed by size-exclusion chromatography (SEC, step 5). In the native nanodisc approach, membrane
943 proteins are purified with amphiphilic copolymers, leaving the membrane protein in a nanodisc that
944 contains endogenous or native lipids (steps 1–3, blue circles). First, cells are incubated with the
945 copolymer (step 1), during which the native nanodiscs form. Next, the protein in native nanodiscs is
946 purified by affinity chromatography (step 2) and SEC (step 3). **b** Chemical structures of MAASTY
947 characterized in this study and AASTY from previous studies[18,38]. MAASTY is composed of MAA (blue)
948 and STY (red), while AASTY

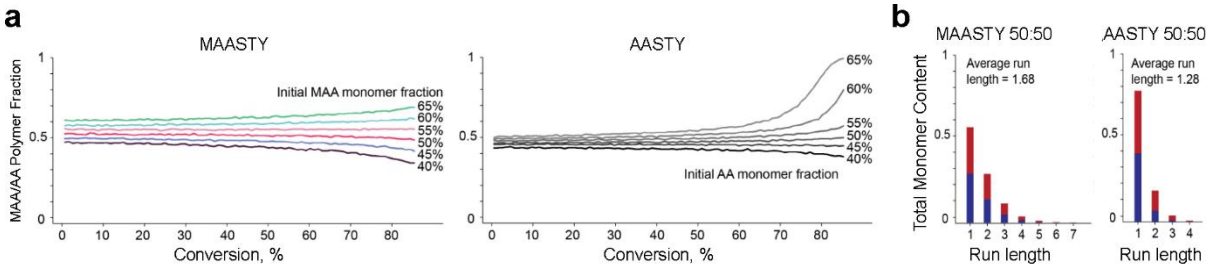

949 is
950 composed by AA (blue) and STY (red).

951

952 **Fig. 2: Simulated composition drift and run length analyses of MAASTY and AASTY copolymers.**
953 **a** MAASTY (left) and AASTY (right) copolymers at six different starting compositions of monomers
954 ranging from 40-65%. X-axes represent the global monomer conversion, and y-axes represent the
955 percentage of MAA or AA copolymerized at the given conversion[40]. All six simulated MAASTY

copolymers were synthesized for this study. **b** Run lengths of MAASTY (left) and AASTY (right) at equimolar MAA or AA to STY copolymerization, with red bars showing STY run lengths, and blue bars showing MAA or AA.

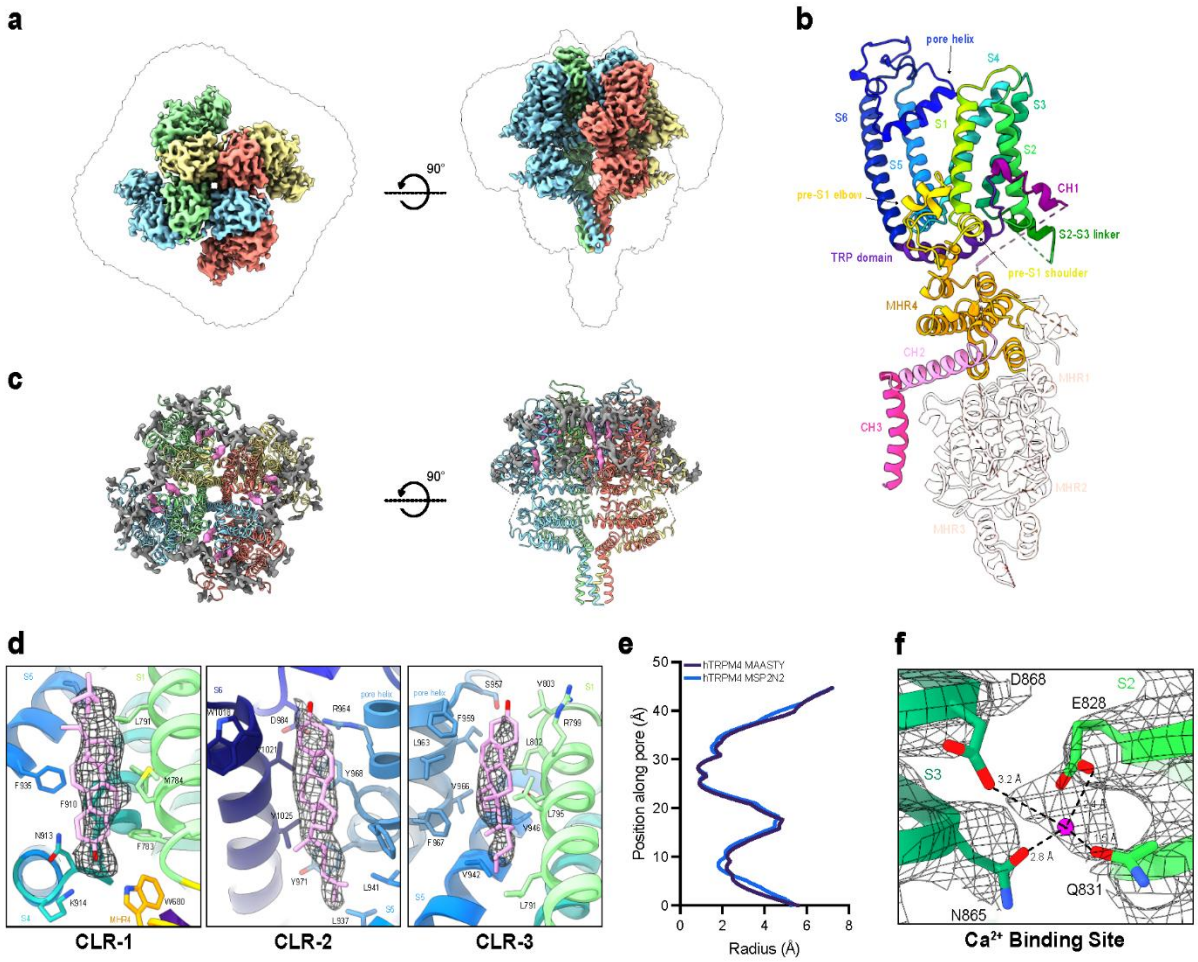

Fig. 3: Structure of hTRPM4 in MAASTY native lipid nanodiscs. a Top and side views of sharpened cryo-EM density maps of hTRPM4 in MAASTY nanodiscs with the four protein subunits colored in light green, salmon, sky blue and khaki overlaid with the unsharpened cryo-EM density map (black outline). The unsharpened map represents the raw reconstruction, showing the full range of densities, including weaker and flexible regions such as copolymers and lipids in the nanodiscs. The sharpened map has been processed with a B-factor of -92 Å² to enhance high-resolution features, improving clarity in well-ordered regions. Contour levels for both maps were adjusted for optimal

967 visualization of key structural features. **b** Atomic model of the monomeric hTRPM4 in MAASTY
968 nanodiscs in ribbons with domains labelled and separately colored. Unresolved domains of MHR1-3 are
969 displayed as transparent ribbons using the atomic model of monomeric hTRPM4 in MSP2N2 nanodiscs. **c**
970 Top and side views of resolved lipid densities among the transmembrane domain of hTRPM4 in
971 MAASTY. The atomic model of hTRPM4 is represented as ribbons and colored as in **a**. Lipid densities
972 are shown in grey and densities characterized as CLR molecules are shown in pink. **d** Close-up views of
973 the positions of identified CLR molecules: CLR-1, CLR-2 and CLR-3, identified in hTRPM4-MAASTY
974 structure. The cryo-EM map densities are represented as mesh and modelled CLR molecules shown as
975 licorice in pink. Domains are labelled and colored as in **c**. **e** Pore profiles of hTRPM4-MAASTY (purple)
976 and hTRPM4-MSP2N2 (blue) structures exhibiting similarly closed states. **f** Identified Ca^{2+} binding site
977 shown as coordination of the bound Ca^{2+} ion by residues Glu^{828}, Gln^{831}, Asn^{865}, and Asp^{868}. Distances are
978 labelled and domains denoted as in **c**.

979 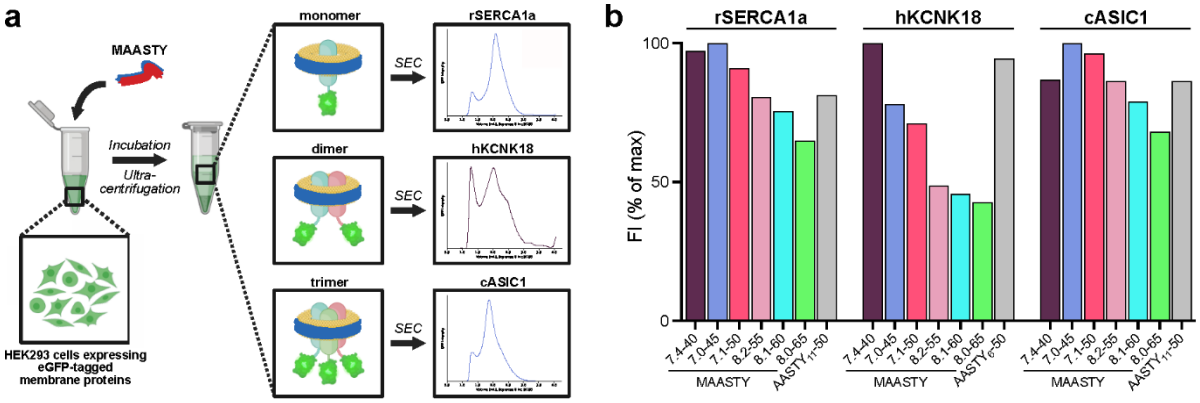

980 **Fig. 4: Solubilization of eukaryotic membrane proteins by MAASTY copolymers. a** Schematic of
981 preparation of MAASTY-solubilized integral membrane proteins from HEK293 cell lysate. First, 2%
982 MAASTY copolymer is added to HEK293 cells recombinantly expressing eGFP-tagged membrane
983 protein and incubated to enable formation of protein-loaded nanodiscs. Insoluble material is then removed
984 via ultra-centrifugation and the soluble fraction is assessed by FSEC using an excitation wavelength of
985 488 nm and emission of 507 nm. In this study, we assessed the solubilization efficiency of MAASTY

copolymers using a test set of membrane proteins including monomeric rSERCA1a, homodimeric hKCNK18, and homotrimeric cASIC1. The displayed example FSEC traces for each test protein (box) represent those with the highest peak intensity at the presumed proteinnanodisc peak. All FSEC traces from all tested copolymers for each membrane protein is found in Fig. S16. Each unique membrane protein copolymer sample was injected twice or more to check reproducibility. **b** Normalized maximum fluorescence intensity values of the protein peaks from the FSEC traces of each tested copolymer to compare differences in solubilization efficiencies. For each protein, the performance of MAASTY copolymers are compared to the best performing AASTY copolymer, as determined by the maximum fluorescence intensity of the presumed protein-nanodisc peak. The maximum fluorescent intensity values of all tested copolymers for each membrane protein is found in Fig. S16.

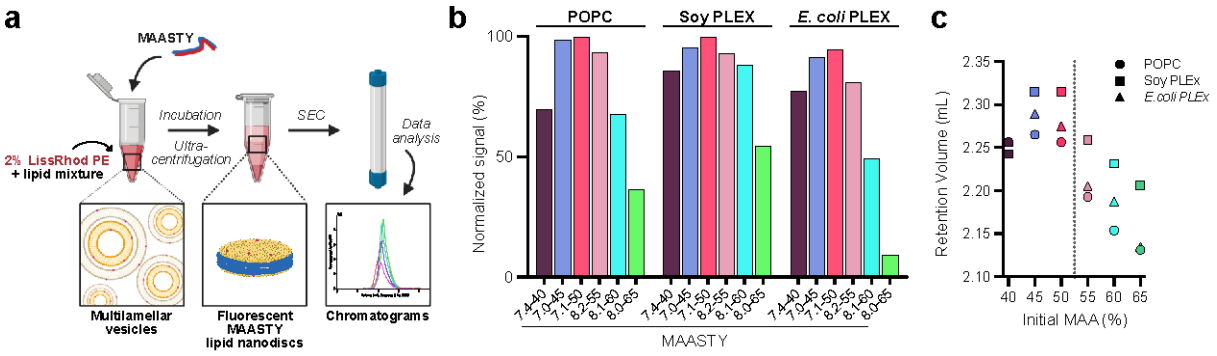

Fig. 5: Solubilization of lipids into nanodiscs by MAASTY copolymers.

a Schematic of preparation of empty native nanodiscs from hydrated lipid films, illustrating the process. First, 2% LissRhod PE is added to a defined lipid composition forming multilamellar vesicles. MAASTY copolymer is added and the mixture and incubated to allow for solubilization. Next, insoluble material is removed via ultra-centrifugation, while the remaining soluble material is assessed by FSEC using an excitation wavelength of 554 nm and emission of 576 nm. Finally, resulting FSEC traces of the tested MAASTY copolymers for differing lipid compositions are compared. **b** Max peak values of the MAASTY-forming empty nanodisc FSEC traces with POPC, Soy PLEx and *E. coli* PLEx mixed with 2% Liss Rhod PE from Fig. S17. Values are normalized relative to the highest detected signal for the

1006 contained data. **c** The retention volumes determined from the max peak values of the MAASTY-forming

1007 empty nanodisc FSEC traces with POPC, soy PLEx and *E. coli* PLEx from Fig. S17 compared to the

1008 initial MAA content (%) of the tested MAASTY copolymers.

1009

Supporting Information

MAASTY: A (dis)ordered copolymer for structural determination of human membrane proteins in native nanodiscs

Ciara F. Pugh,[†] Lukas P. Feilen,[†] Dušan Živković,[‡] Kaia F. Præstegaard,[¶] Charalampos Sideris,[¶,†] Neil J. Borthwick,[¶] Casper de Lichtenberg,[†] Jani R. Bolla,[‡] Anton Allen Abbotsford Autzen,[*,¶] and Henriette Elisabeth Autzen[*,†]

†*Department of Biomedical Sciences, University of Copenhagen, Copenhagen N, DK-2200, Denmark*

‡*Department of Biology, University of Oxford, Oxford, OX1 3RB, United Kingdom*

¶*Department of Health Technology, Technical University of Denmark, Kgs. Lyngby, DK-2800, Denmark*

E-mail: aaas@dtu.dk; henriette.autzen@sund.ku.dk

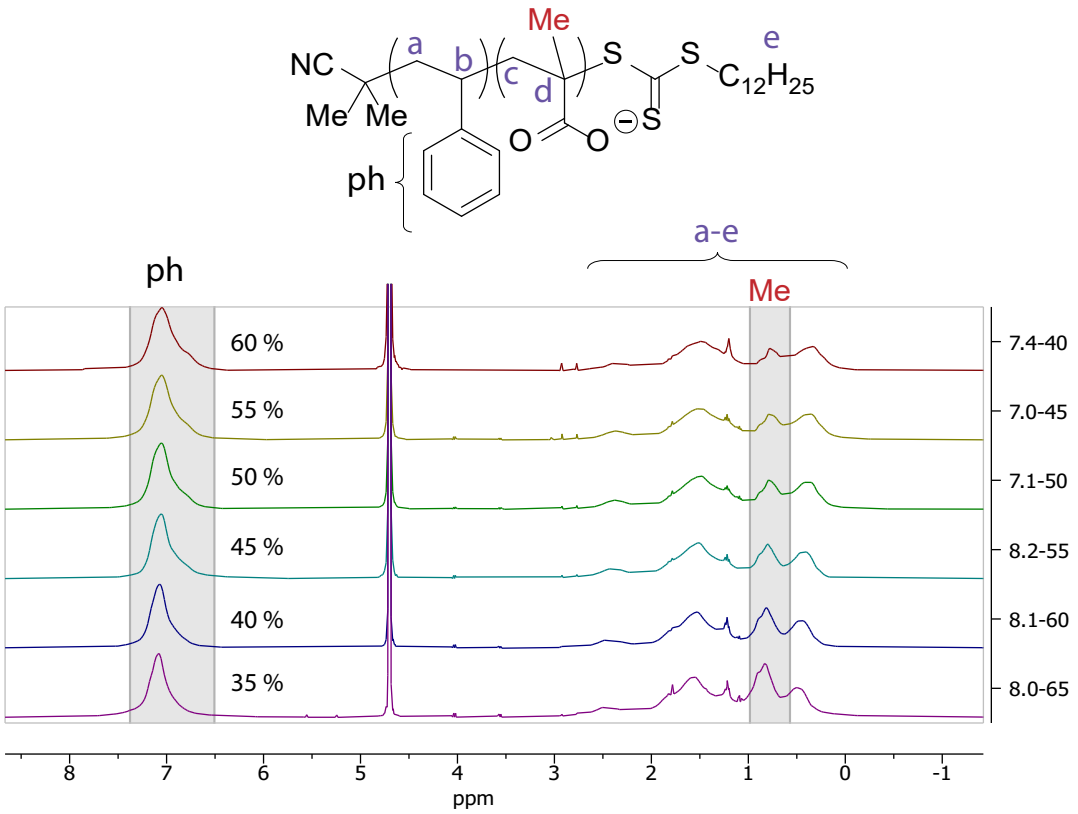

Figure S1: ^{1}H-NMR of MAASTY copolymers. ^{1}H-NMR (D_2O, 400 MHz): δ [ppm] = 7.5 - 6.5 (phenyl H), 3.0 - 0.3 (aliphatic H). STY content is seen in the part of the spectrum marked by ph (shaded in grey, curly brackets in structure). The shoulder at 6.8 ppm arises from an increase in adjacent STY-STY monomers with increasing STY content, which changes the local chemical environment for the protons in the phenyl. The methyl signal from MAA is seen to increase in proportion with MAA content in the part of the spectrum marked by Me (shaded in grey, red in structure). The MAA content is in correspondence with the initial feed of MAA.

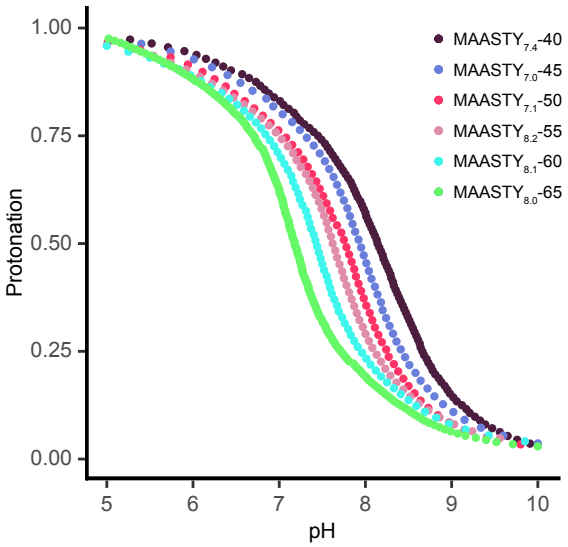

Figure S2: Bjerrum diagram of MAASTY copolymers describing copolymer pKa and pH tolerance. Bjerrum diagrams were constructed by dissolving 50 mg of each MAASTY copolymer in 10 mL water and adjusting the pH to approximately 11 with 1 M NaOH. The pH was measured on a Mettler Toledo SevenCompact S210 pH meter while 0.33 M HCl solution was titrated in 5 µL increments into the dissolved copolymer solution.

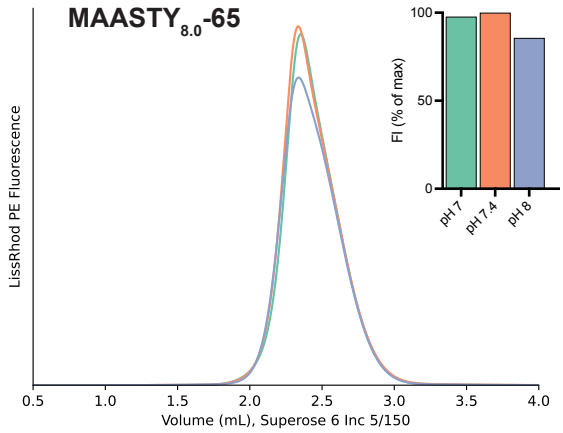

Figure S3: MAASTY$_{8.0}$-65 solubilization of lipid vesicles at different pH. Fluorescent, protein-free nanodiscs were produced as described in methods and as illustrated in Fig. 5a. Raw FSEC traces of protein-free nanodiscs generated by solubilizing 1 mM POPC with 2% fluorescent LissRhod PE lipid vesicles with 1% (w/v) of MAASTY$_{8.0}$-65 in specified pH. Samples were injected onto a Superose 6 Increase 5/150 gel filtration column and detected for LissRhod PE with excitation at 554 nm and emission at 576 nm. Insert bar graph represents maximum fluorescence intensities of the traces, normalized to maximum detected peak intensity. Each bar represents a single data point.

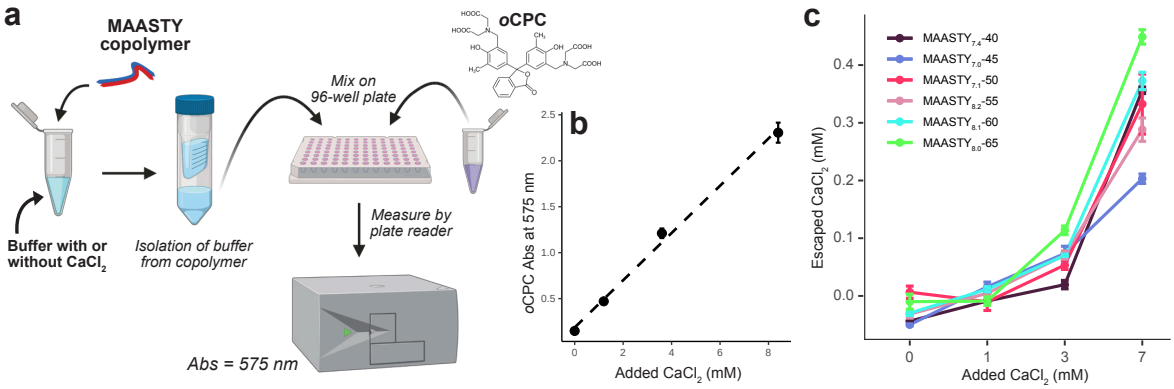

Figure S4: Assessment of Ca^{2+} sensitivity of MAASTY copolymers with o-cresolphthalein complexone (oCPC). a Schematic representation of the assay. Tested MAASTY copolymers were solubilized and mixed in buffers of examined $CaCl_2$ concentrations. Buffer was then isolated from the copolymer using a 10 kDa MWCO centrifugal concentrator and mixed with oCPC in a 96-well plate. Finally, absorbance at 575 nm was measured in a plate reader to calculate free Ca^{2+} concentration. **b** Standard curve of measured oCPC in increasing $CaCl_2$ concentrations. Data points represent triplicate measurements ± standard deviation (SD, error bars), $R^2 = 0.995$. **c** Free Ca^{2+} concentration in solution following exposure to 1% MAASTY copolymer as measured using oCPC. Data points represent triplicate measurements ± SD (error bars).

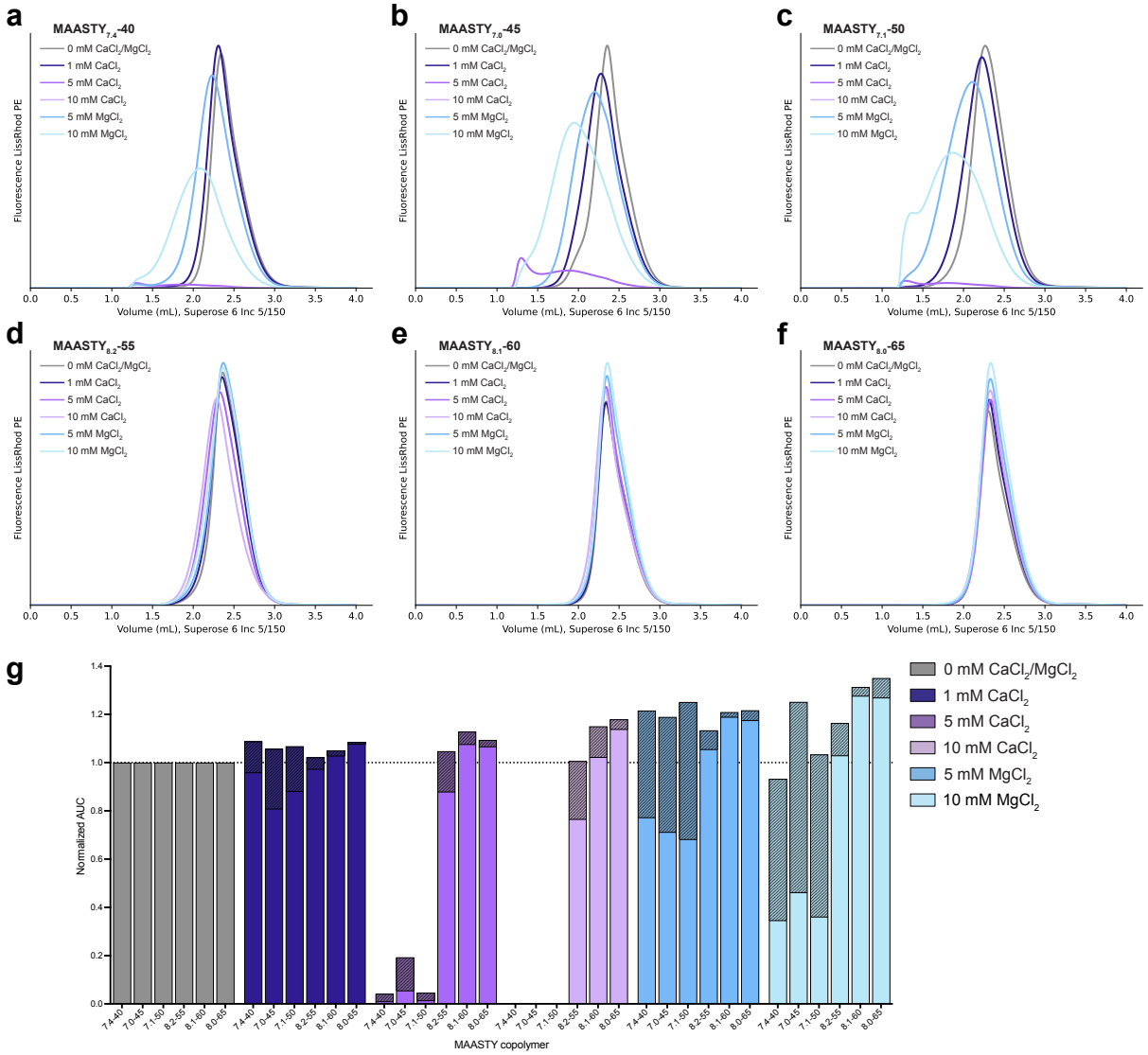

Figure S5: Solubilization of lipid vesicles by MAASTY copolymers in the presence of divalent cations. Fluorescent, protein-free nanodiscs were produced as described in methods and as illustrated in Fig. 5a. **a-f** Raw FSEC traces of protein-free nanodiscs generated by solubilizing 1 mM POPC with 2% fluorescent LissRhod PE lipid vesicles with 1% (w/v) of a given MAASTY copolymer in the presence of specified $CaCl_2$ and $MgCl_2$ concentrations. Samples were injected onto a Superose 6 Increase 5/150 gel filtration column and detected for LissRhod PE with excitation at 554 nm and emission at 576 nm. **g** Analysis of area under the curve (AUC) for the nanodisc peak which elutes at a retention volume of ∼2.3 mL. Each datapoint is normalized to the AUC of the 0 mM $CaCl_2/MgCl_2$ condition for each respective MAASTY copolymer. The nanodisc-containing peak for each condition was determined as that which overlaps with the 0 mM divalent cation condition (solid color). Bar sections with a diagonal line fill represent the larger, soluble species determined as AUC from a lower retention volume than the 0 mM divalent cation condition. Each bar represents a single datapoint.

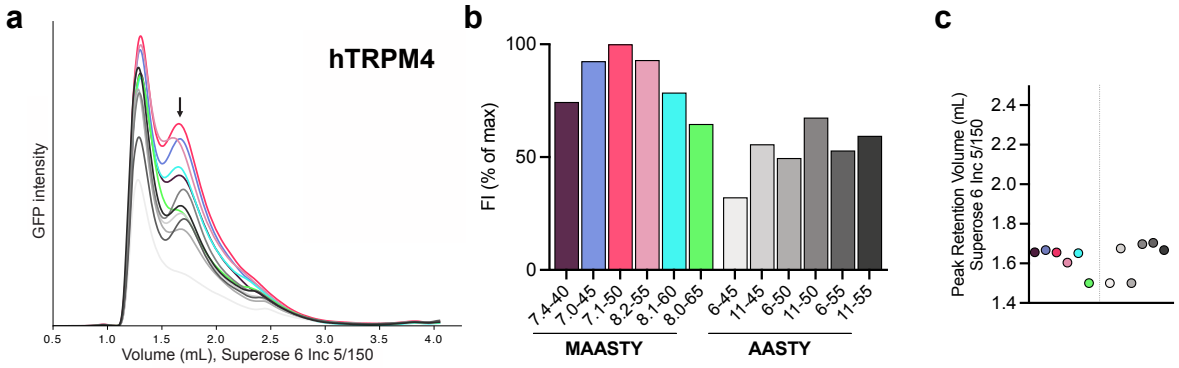

Figure S6: Solubilization of hTRPM4 in MAASTY copolymers. **a** Raw FSEC traces of hTRPM4 solubilized by the MAASTY library presented in this study and for comparison the AASTY library presented in Smith *et al.*[1]. The samples were injected onto a Superose 6 Increase 5/150 gel filtration column and detected for eGFP using an excitation wavelength of 488 nm and emission of 507 nm. From the chromatogram, a void peak is seen at approximately 1.2 mL with the presumed protein-nanodisc peak denoted by an arrow. **b** Maximum fluorescence intensities of the traces in **a**, normalized to maximum detected peak intensity. **c** Peak retention volumes of the traces in **a**. Each unique membrane protein copolymer sample was injected twice or more to check reproducibility.

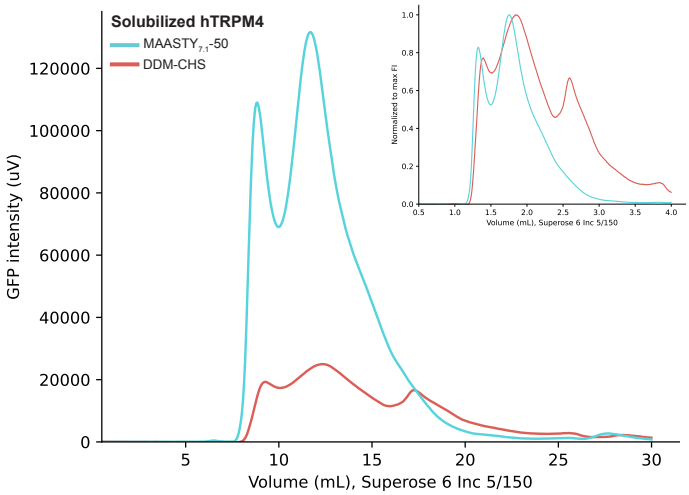

Figure S7: Solubilization comparison of hTRPM4 by MAASTY$_{7.1}$-50 and DDM-CHS. Raw FSEC traces of hTRPM4 solubilized by 2% (w/v) MAASTY$_{7.1}$-50 (blue) and 20 mM DDM with 4 mM CHS (red). The samples were injected onto a Superose 6 Increase 5/150 gel filtration column equilibrated in HBS or buffer containing 100 mM NaCl, 0.5 mM DDM and 20 mM HEPES/NaOH, pH 7.4 for the MAASTY or DDM-CHS conditions, respectively, and detected for eGFP using an excitation wavelength of 488 nm and emission of 507 nm. Insert represents each trace normalized to maximum GFP intensity showing the distribution of each trace.

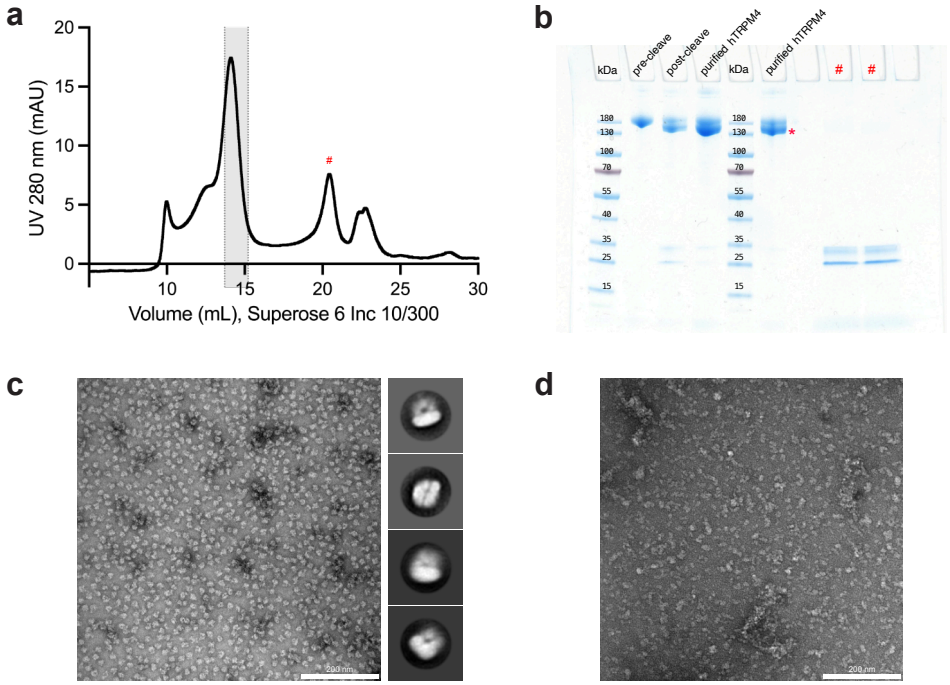

Figure S8: Purification of hTRPM4 in MAASTY lipid nanodiscs. a Chromatogram of absorbance at 280 nm of purified hTRPM4 in MAASTY native nanodiscs from Superose 6 Increase 10/300 gel filtration column. Sample fractions (highlighted in grey) were pooled and concentrated for structural determination of hTRPM4 in MAASTY by cryo-EM. The peak at 10 mL and shoulder at ∼12.5 mL derive from the void and heterogeneous aggregates of hTRPM4, respectively. The peak at 20 mL contains TEV protease and the StrepTagII-eGFP tag as analyzed by SDS-PAGE in **b** in the lanes denoted by #. **b** SDS-PAGE analysis of hTRPM4-containing MAASTY native nanodiscs representing (from left to right): hTRPM4-MAASTY before the addition of TEV protease, hTRPM4-MAASTY after O/N cleavage by TEV protease, purified hTRPM4 in MAASTY native nanodiscs for downstream analyses (repeated), 2 fractions from the peak denoted by # in **a**. The protein band at ∼134 kDa represents the proteomer of hTRPM4 in MAASTY nanodiscs and is marked by *. The faint band above is partially uncleaved purified hTRPM4 in MAASTY as identified by in-gel fluorescence (data not shown).**c** Negative stain TEM image of hTRPM4-MAASTY with representative 2D classes. **d** Negative stain TEM image of MAASTY-solubilized HEK293F membranes expressing hTRPM4.

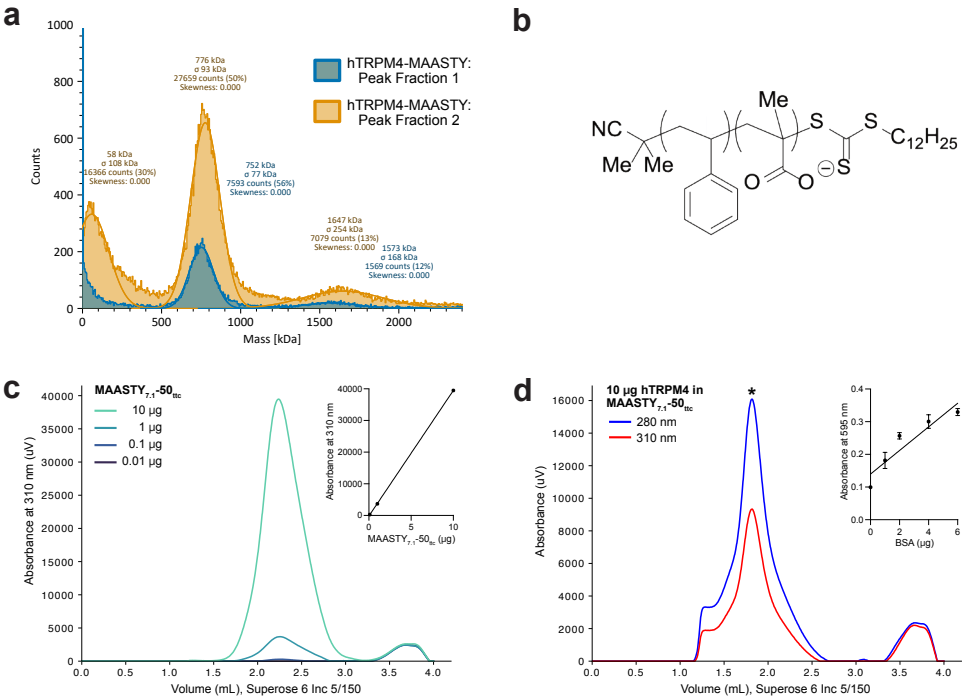

Figure S9: Compositional analysis of hTRPM4 in MAASTY lipid nanodiscs. **a** Mass photometry analysis of peak fractions from purification of hTRPM4 in MAASTY nanodiscs as shown in Fig. S8a. Two 500 μL fractions of purified hTRPM4-MAASTY were collected and analyzed. Peak fraction 1 (blue) comprises the majority of the protein peak with hTRPM4-MAASTY likely representing the 760 kDa species, whereas peak fraction 2 (orange) comprises the right-side of the peak (larger retention volume) as evident by the higher abundance of smaller species. **b** Molecular structure of MAASTY copolymer with the trithiocarbonate (ttc) moeity (RAFT reagent), which has a maximum absorbance of 310 nm. **c** Raw SEC traces of specified masses of MAASTY$_{7.1}$-50$_{ttc}$ copolymer injected on to a Superose 6 Increase 5/150 gel filtration column and measured at 310 nm absorbance. Insert represents a standard curve derived from the maximum intensity values from the copolymer peak ($\sim$2.3 mL retention volume). **d** Raw SEC traces from the injection of 10 μg purified hTRPM4 in MAASTY$_{7.1}$-50$_{ttc}$ lipid nanodiscs on to a Superose 6 Increase 5/150 gel filtration column measured at 280 nm (blue) and 310 (red) nm absorbance, representing total protein and MAASTY$_{7.1}$-50$_{ttc}$ copolymer, respectively. Insert represents a BSA standard curve from the Bradford protein assay used to determine the concentration of purified hTRPM4 in MAASTY$_{7.1}$-50$_{ttc}$ lipid nanodiscs prior to SEC.

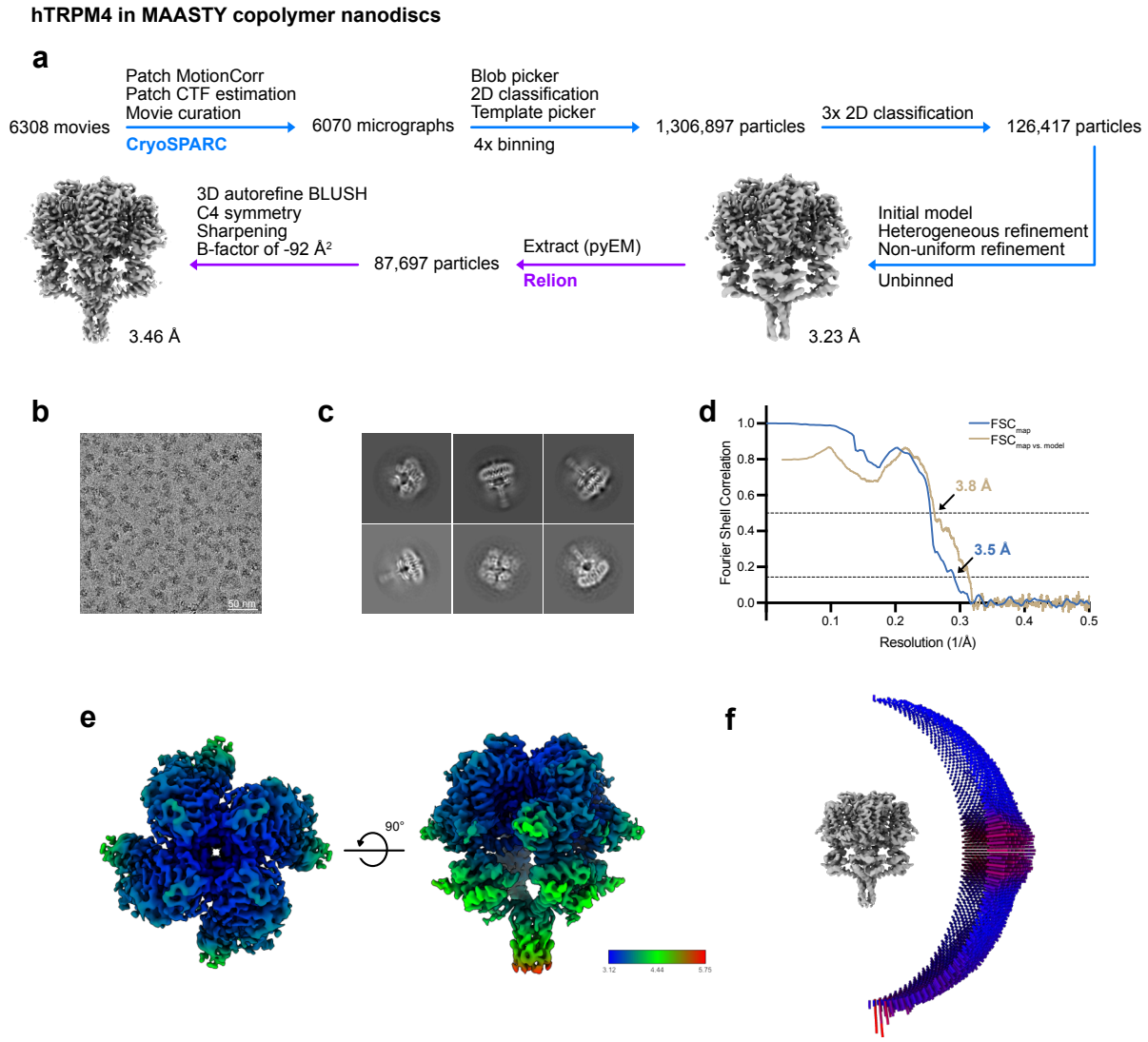

Figure S10: Cryo-EM data processing of hTRPM4 in MAASTY lipid nanodiscs. **a** Cryo-EM data processing pipeline for hTRPM4 in MAASTY. Motion correction, CTF estimation, particle picking, 2D classification and primary refinement steps were carried out in CryoSPARC[2] (blue arrows). Refined particles were then re-extracted in Relion 5.0[3] after particle stack conversion by pyEM[4], and refined using BLUSH regularization[5] (purple arrows). Despite an overall slightly lower estimated resolution, the reconstructions obtained from refinement in Relion 5.0 with BLUSH regularization and sharpening showed higher occupancy and better-resolved cytosolic domains than the map determined from non-uniform refinement in CryoSPARC. This led us to continue with the Relion 5.0 reconstructions, with an estimated overall resolution of 3.46 Å, for further analyses. **b** Representative motion-corrected micrograph imaged at 165,000x magnification. **c** Representative 2D class averages. **d** Fourier shell correlation (FSC) half-map and model-map curves, adopted from Relion 5.0 and Phenix Mtriage[6], respectively. The gold standard FSC curve from the two half maps (FSC_{map}) is shown in blue with resolution at FSC = 0.143 indicated by an arrow. The FSC curve generated from the map and atomic model ($FSC_{map\ vs.\ model}$) is shown in brown with resolution at FSC = 0.5 indicated by an arrow. **e** Local resolution representation of the best reconstruction. **f** Angular distribution of particles used in the final reconstruction.

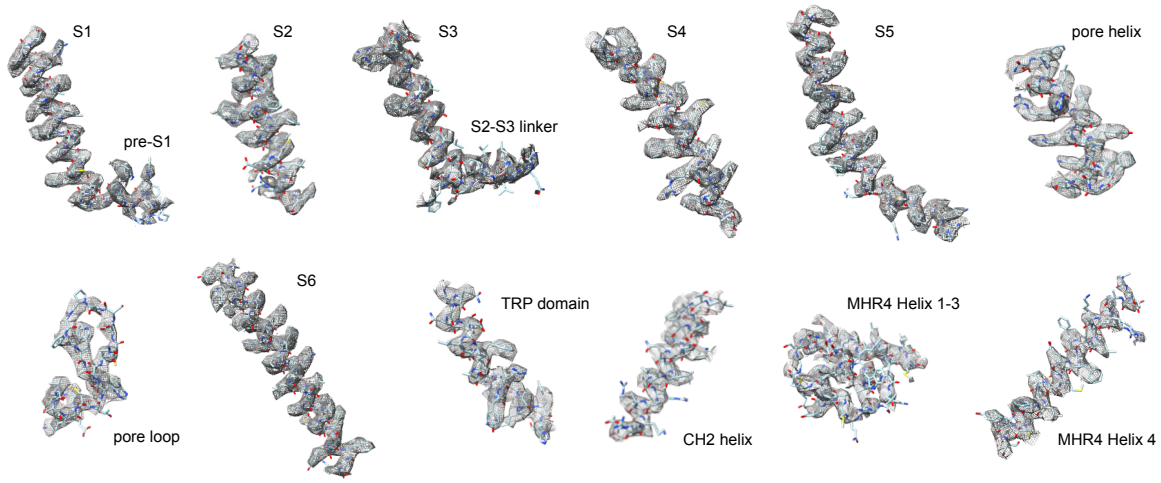

Figure S11: Representative regions from the best reconstruction of hTRPM4 in MAASTY nanodiscs. Shown are representative labelled segments of hTRPM4 with the fitted atomic model.

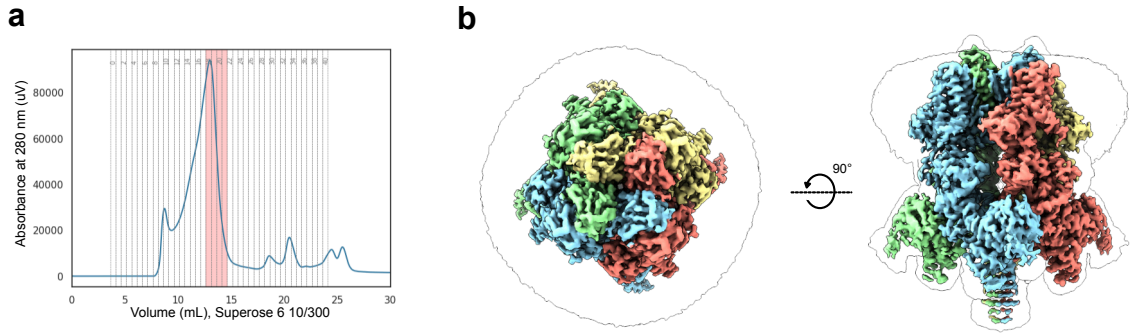

Figure S12: Purification and structural determination of hTRPM4 in MSP2N2 reconstituted nanodiscs. a Chromatogram of absorbance at 280 nm of purified hTRPM4 in MSP2N2 nanodiscs from Superose 6 Increase 10/300 gel filtration column. Sample fractions (highlighted in red) were pooled and concentrated for structural determination of hTRPM4 in MSP2N2 by cryo-EM. **b** Side and top views of sharpened cryo-EM density maps of hTRPM4 in MSP2N2 reconstituted nanodiscs with the four protein subunits colored in light green, salmon, sky blue and khaki, overlaid with the unsharpened cryo-EM density map (black outline). The unsharpened map represents the raw reconstruction, showing the full range of densities, including weaker and flexible regions such as copolymers and lipids in the nanodiscs. The sharpened map has been processed with a B-factor of -147 $Å^2$ to enhance high-resolution features, improving clarity in well-ordered regions. Contour levels for both maps were adjusted for optimal visualization of key structural features.

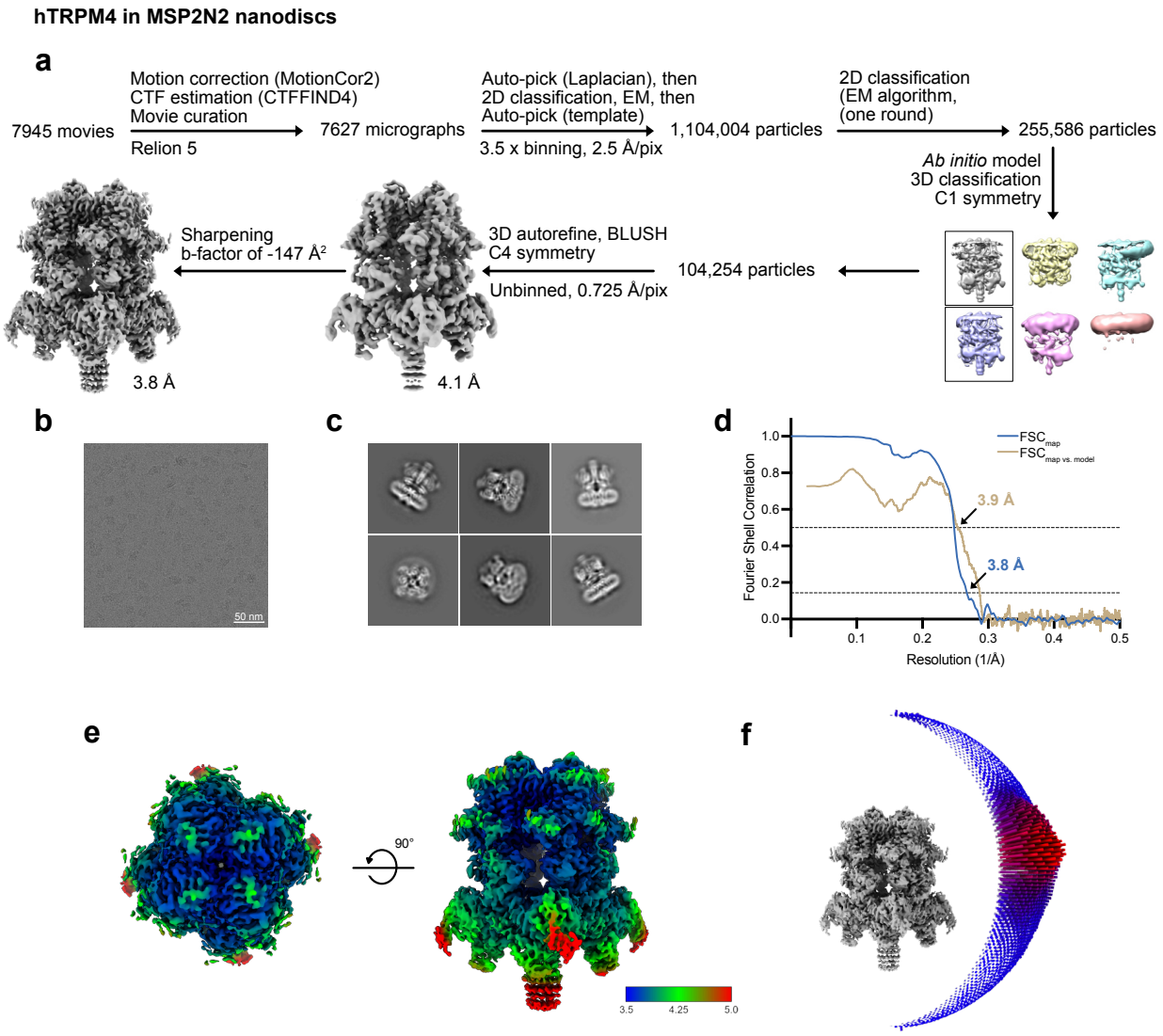

Figure S13: Cryo-EM data processing of hTRPM4 reconstituted in MSP2N2 lipid nanodiscs. **a** Cryo-EM data processing pipeline for hTRPM4 in MSP2N2. Motion correction, CTF estimation, particle picking, 2D classification, 3D classification and 3D refinement were carried out in Relion 5.0[3]. Blush regularization was applied during 3D refinement[5]. **b** Representative motion-corrected micrograph imaged at 165,000x magnification. **c** Representative 2D class averages. **d** Fourier shell correlation (FSC) half-map and model-map curves, adopted from Relion 5.0 and Phenix Mtriage[6], respectively. The gold standard FSC curve from the two half maps (FSC_{map}) is shown in blue with resolution at FSC = 0.143 indicated by an arrow. The FSC curve generated from the map and atomic model ($FSC_{map\ vs.\ model}$) is shown in brown with resolution at FSC = 0.5 indicated by an arrow. **e** Local resolution representation of the best reconstruction. **f** Angular distribution of particles used in the final reconstruction.

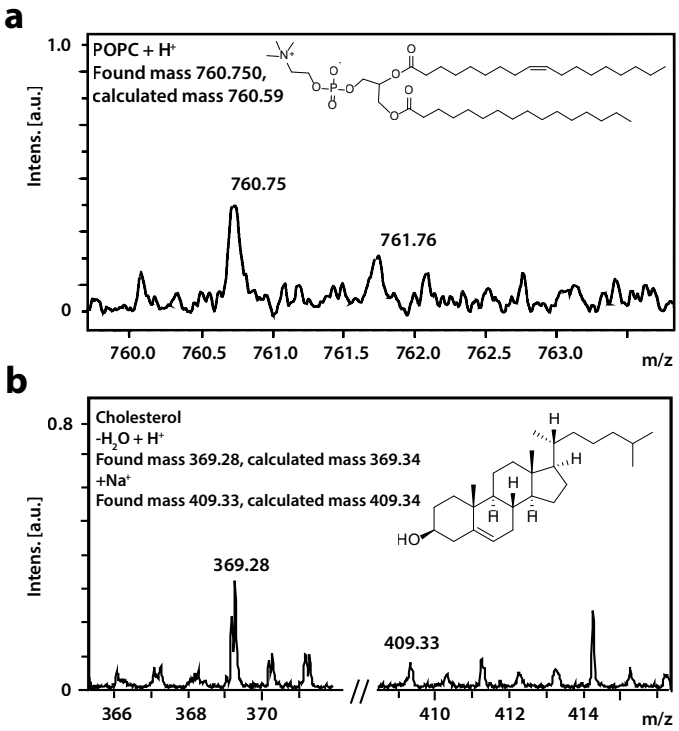

Figure S14: Analysis of lipids co-purified with hTRPM4 in MAASTY lipid nanodiscs by MALDI-TOF mass spectrometry. Representative spectra of identified lipids: POPC (**a**) and cholesterol (**b**).

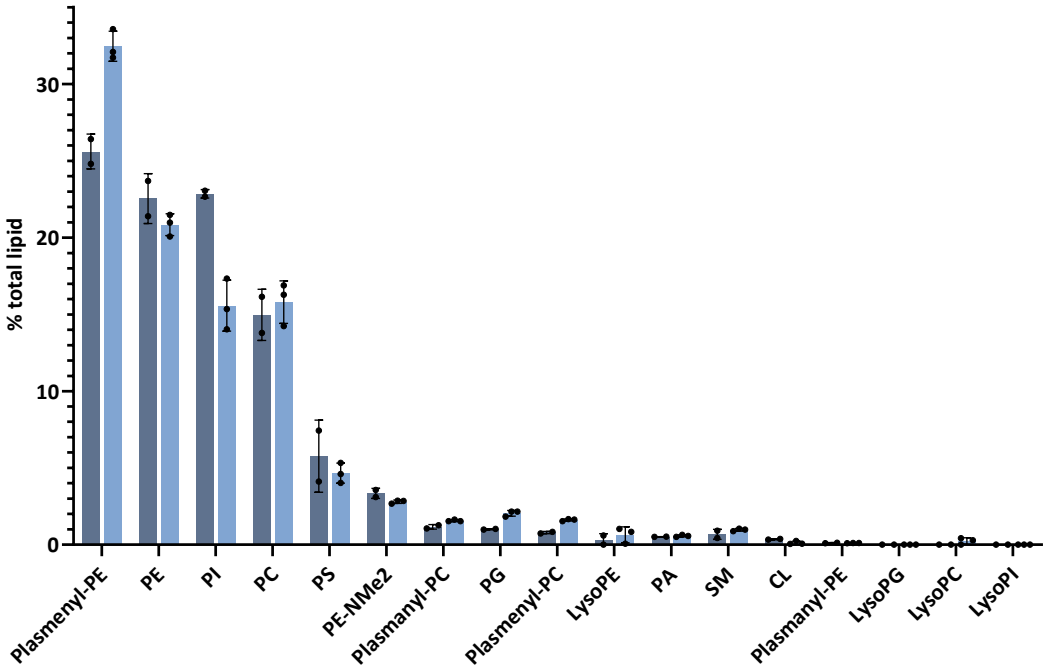

Figure S15: Lipidomics analysis of hTRPM4 in MAASTY lipid nanodiscs. Bar graphs show the relative abundance of phospholipids from the purified hTRPM4 lipid microenvironment analyzed from two separate protein expressions and purifications (grey and blue bars) with two and three technical replicates, respectively. Error bars represent ± SD. The phospholipids, PE, PI, PC and PS constituted the majority of observed lipid species. All the lipid types observed in the lipidomics analysis are supplied as Source Data.

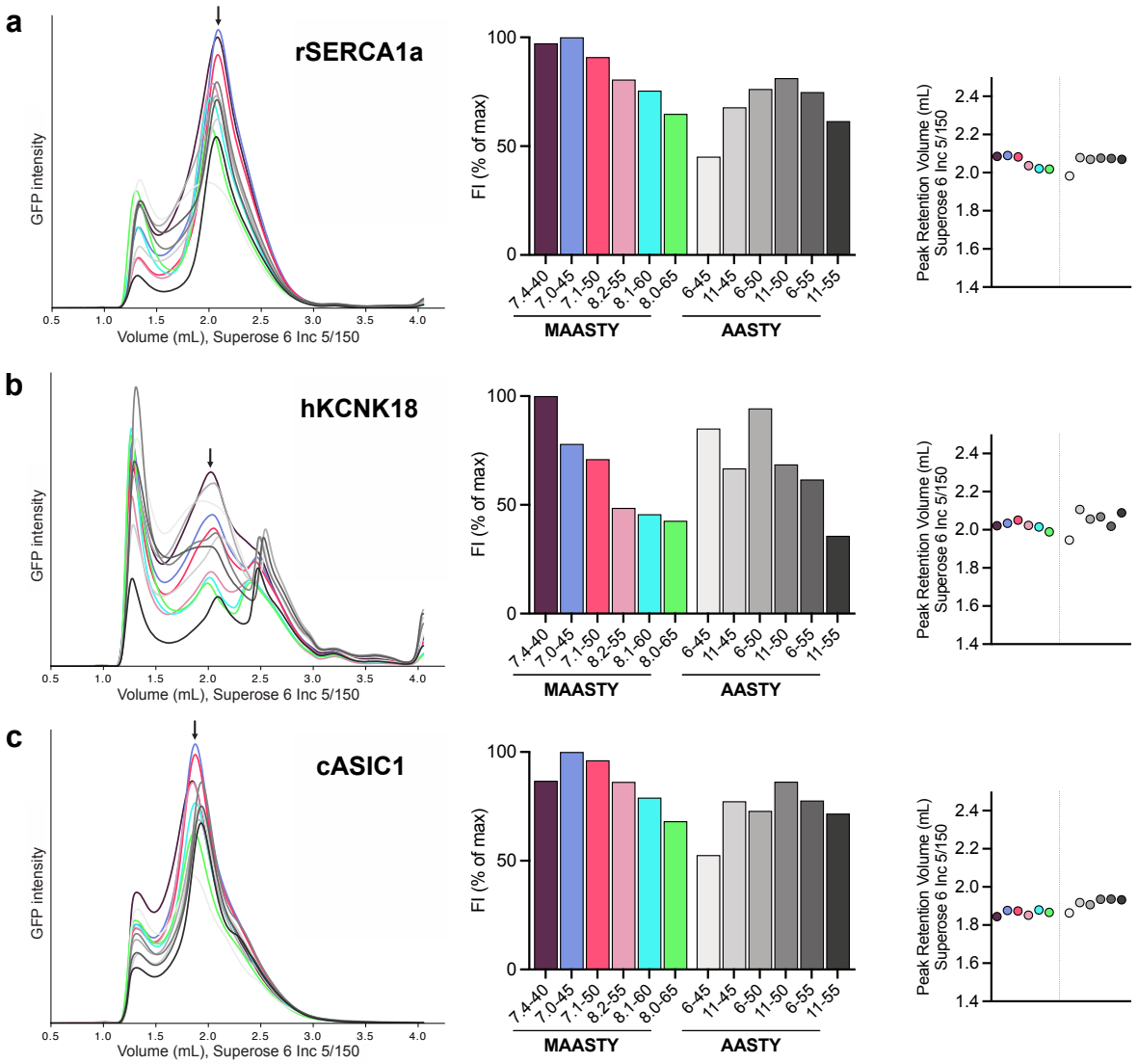

Figure S16: Solubilization of rSERCA1a (a), hKCNK18 (b), and cASIC1 (c) with MAASTY and AASTY copolymers, as examined by FSEC. All membrane proteins were recombinantly expressed with an eGFP fusion tag. The samples were injected onto a Superose 6 Increase 5/150 gel filtration column and and detected for eGFP with excitation at 489 nm and emission at 507 nm. The first column shows raw FSEC traces with a void peak around 1.2 mL, and arrows that denote the presumed protein-nanodisc peak. The second column displays the maximum fluorescence intensities of the denoted protein-nanodisc peak, normalized to maximum detected peak intensity. The third column exhibits peak retention volumes. Each unique membrane protein copolymer sample was injected twice or more to check reproducibility.

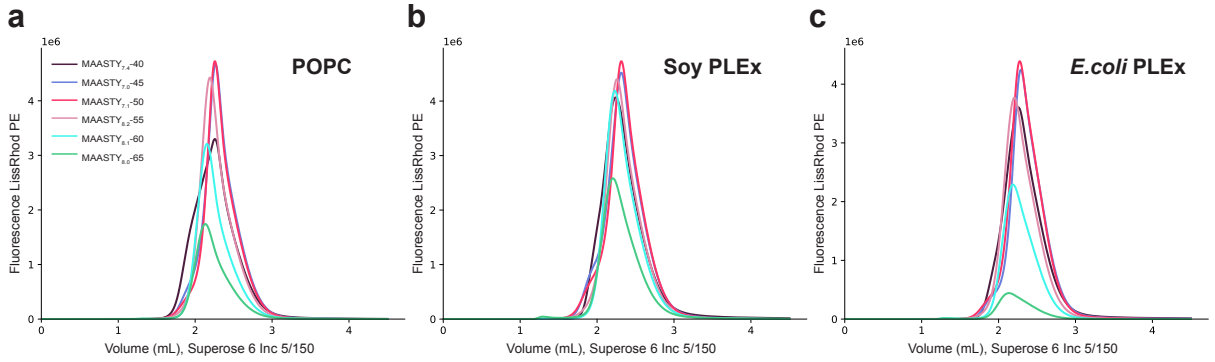

Figure S17: Solubilization of lipids into nanodiscs by MAASTY copolymers. FSEC traces of MAASTY-stabilized empty nanodiscs with the following lipids: POPC (**a**), Soy PLEx (**b**), and *E. coli* PLEx (**c**), mixed with 2% LissRhod PE with excitation at 554 nm and emission at 576 nm.

Supplementary Table 1: Data acquisition and processing, modelling statistics and validation scores.

	hTRPM4 in MAASTY	**hTRPM4 in MSP2N2**
Data collection		
Pixel size (Å)	0.749/0.725	0.725
Dose ($e^{-}Å^2$)	52	52
Defocus range (µm)	0.5-2.5	0.5-2.5
Total micrographs	6308	7945
Data processing		
Curated micrographs	6070	7627
Picked particles	1,306,897	1,104,004
Selected particles (post 2D)	126,417	255,586
Selected particles (post 3D)	87,697	103,254
Map resolution (Å)	3.46	3.78
Map sharpening B factor ($Å^2$)	-92	-147
Model refinement		
Protein residues	558-711, 767-835, 850-1089, 1107-1108, 1116-1166	558-711, 767-835, 842-1094, 1107-1181
Ligands (pr. chain)	3 CLR, 1 Ca^{2+}	3 CHS, 1 Ca^{2+}
R.M.S. deviations		
Length (Å)	0.002	0.002
Angles (°)	0.531	0.618
Ramachandran		
Favored (%)	96.21	93.30
Allowed (%)	3.79	6.70
Outliers (%)	0.00	0.00
Model validation		
MolProbity score	1.70	2.37
Clash score	8.22	11.06
Rotamer outliers (%)	0.57	3.15
Rama-Z score	1.23	0.01

Supplementary Table 2: Overview of AASTY copolymers used in this study. Abbreviations: acrylic acid, AA; number-average molecular weight, M_n.

Nomenclature	Initial AA (%)	M_n (kDa)
$AASTY_6$-45	45	6
$AASTY_{11}$-45	45	11
$AASTY_6$-50	50	6
$AASTY_{11}$-50	50	11
$AASTY_6$-55	55	6
$AASTY_{11}$-55	55	11

References

(1) Smith, A. A.; Autzen, H. E.; Faust, B.; Mann, J. L.; Muir, B. W.; Howard, S.; Postma, A.; Spakowitz, A. J.; Cheng, Y.; Appel, E. A. Lipid Nanodiscs via Ordered Copolymers. *Chem* **2020**, *6*, 2782–2795, DOI: 10.1016/j.chempr.2020.08.004.

(2) Punjani, A.; Rubinstein, J. L.; Fleet, D. J.; Brubaker, M. A. cryoSPARC: algorithms for rapid unsupervised cryo-EM structure determination. *Nature Methods* **2017**, *14*, 290–296, DOI: 10.1038/nmeth.4169.

(3) Burt, A.; Toader, B.; Warshamanage, R.; von Kügelgen, A.; Pyle, E.; Zivanov, J.; Kimanius, D.; Bharat, T. A. M.; Scheres, S. H. W. An image processing pipeline for electron cryo-tomography in RELION-5. *FEBS Open Bio* **2024**, *14*, 1788–1804, DOI: 10.1002/2211-5463.13873.

(4) Asarnow, D.; Palovcak, E.; Cheng, Y. UCSF pyem v0.5. *Zenodo* **2019**, DOI: https://doi.org/10.5281/zenodo.3576630.

(5) Kimanius, D.; Jamali, K.; Wilkinson, M. E.; Lövestam, S.; Velazhahan, V.; Nakane, T.; Scheres, S. H. W. Data-driven regularisation lowers the size barrier of cryo-EM structure determination. *bioRxiv* **2023**, DOI: 10.1101/2023.10.23.563586.

(6) Afonine, P. V.; Klaholz, B. P.; Moriarty, N. W.; Poon, B. K.; Sobolev, O. V.; Terwilliger, T. C.; Adams, P. D.; Urzhumtsev, A. New tools for the analysis and validation of cryo-EM maps and atomic models. *Acta Crystallographica Section D: Structural Biology* **2018**, *74*, 814–840, DOI: 10.1107/S2059798318009324.